HyQu

Designing Acoustic Mode Shapes for Microwave to Optical Transduction

Master's Thesis

Alexandra Carmen Bernasconi

`alexandra.bernasconi@bluewin.ch`

Supervisors:
Prof. Yiwen Chu
Tom Schatteburg

February 1, 2021

Abstract

To date, various systems are being studied and developed that operate at the quantum limit. These systems provide versatile opportunities for quantum sensing and quantum computation: Fast and high-fidelity single and two-qubit gates have been implemented using superconducting qubits [1] where on the other side, low propagation loss of quantum signals at room temperature can be implemented using optical photons [2]. Thus, combining different systems would allow one to benefit from each system's unique advantages. To couple these systems in a useful way, reliable microwave-to-optical transduction is needed.

Recent work has demonstrated that phonon modes in high-overtone bulk acoustic wave resonators (HBARs) are promising candidates for mediating quantum states between microwave and optical photons [3–8]. Yet, the use of an interim state requires the optimization of transduction to both the microwave and the optical photon states: To achieve reliable transduction between the microwave photon and the HBAR-phonon mode, we must maximize the piezoelectric coupling between them, and to obtain reliable transduction between the optical photons and the HBAR-phonon mode, we need to maximize the Brillouin-like optomechanical coupling. As we therefore want to couple an optical infrared (IR) laser and a superconducting antenna to the same HBAR-phonon mode, a major challenge remains to avoid exposing the antenna to IR laser light. Indeed, infrared light on superconductors leads to quasiparticles, which have various unwanted side effects.

In this work, we discuss various phonon mode shapes in HBARs that can enable simultaneous coupling to infrared laser light and microwaves. We discuss in detail the couplings of the (1,0)-Laguerre-Gaussian (LG) mode in combination with a ring-shaped superconducting microwave antenna and the couplings of the (1,0)-Hermite-Gaussian (HG) modes in combination with a circle superconducting microwave antenna. We will compare both mode shapes regarding their coupling strengths and their infrared irradiation on the antenna and show that the (1,0)-LG mode appears more promising in this regard.

Contents

Contents

Introduction

In a strongly interconnected society where fake news and trolling influence politicians' agendas, there is a need for high-security information channels. In fact, confidentiality is one of the main requirements in peace mediation processes [9]. Quantum technology offers the possibility of inherently private communication channels, and constructing a quantum internet lays the foundation for this.

Also, Richard Feynman claimed in the 1980s that the use of quantum computers would simplify problem solving in physics, chemistry, and biology [10]. Various approaches are being considered in research on the realization of quantum computers and each one has its unique advantages. It has recently been shown that superconducting qubits could provide a powerful basis for building quantum computers and quantum computing nodes [1]. Yet, the microwave signals from superconducting qubits are not suitable for long-distance transmission. For a practical use of superconducting quantum processors, long-distance transport of quantum states will be of great importance. Therefore, the ability to transduce a microwave quantum signal into an optical photon will become essential in the near future.

For implementing microwave to optical transduction, recent work suggests the use of high-overtone bulk acoustic wave resonator (HBAR)-phonon modes [3–8]. Microwave states can be transduced into phonon states of the HBAR by piezoelectric coupling. From there, the phonon states can be read out into optical infrared (IR) photons using Brillouin-like optomechanical coupling. The reverse path from the IR photons to the microwave signal works with the same coupling mechanisms. In the center of Figure 1.1, we show a planned experimental setup for the transduction experiment. The HBAR is placed around an optical cavity, which enables the optomechanical coupling and the piezoelectric material on the HBAR enables the electromechanical coupling to the antenna of the superconducting qubit.

In performing the transduction experiment, we must be careful of two things. First, the antenna must not disturb the cavity field. Second, as we aim to couple to the same acoustic mode with an infrared laser and a superconducting antenna, we need to consider the effects of IR light on the superconducting antenna. Radiation of IR light onto superconductors breaks Cooper pairs and creates quasiparticles. As the density of quasiparticles rises above the one of Cooper pairs, superconductivity breaks down. But already at lower concentrations, quasiparticles significantly degrade the coherence time of qubits [11]. Hence, we seek to protect the superconducting antenna from IR radiation as much as possible.

While we want to keep the IR radiation on the antenna low, we also want to make the

two couplings to the HBAR phonon mode as strong as possible. This work focuses on understanding what is needed to achieve this. In the beginning we will give an overview of relevant physical concepts such as phonon modes, piezoelectric coupling, Brillouin-like optomechanical coupling and quasiparticles. We will then explain the planned device design and how we simulate acoustic modes inside the HBAR. In chapter 5 we will focus on two acoustic mode shapes - the (1,0)-Hermite Gaussian (HG) mode and the (1,0)-Laguerre Gaussian (LG) mode - and explore their qualities in terms of coupling strengths and avoiding quasiparticles.

We must remember, however, that the full transduction process depends on multiple interdependent factors. Figure 1.1 shows our strategy to find optimized transduction parameters. We chose to set the the goals circled in red: Increasing electromechanical coupling rate, increasing optomechancial coupling rate and decreasing quasiparticle generation rate on the antenna. These are not the only limiting factors in the transduction process, but we will focus on them for now. To achieve these set goals, we intend to adjust three factors: the superconducting antenna, the IR laser cavity mode and the acoustic HBAR mode. In Figure 1.1, these are shown in blue.
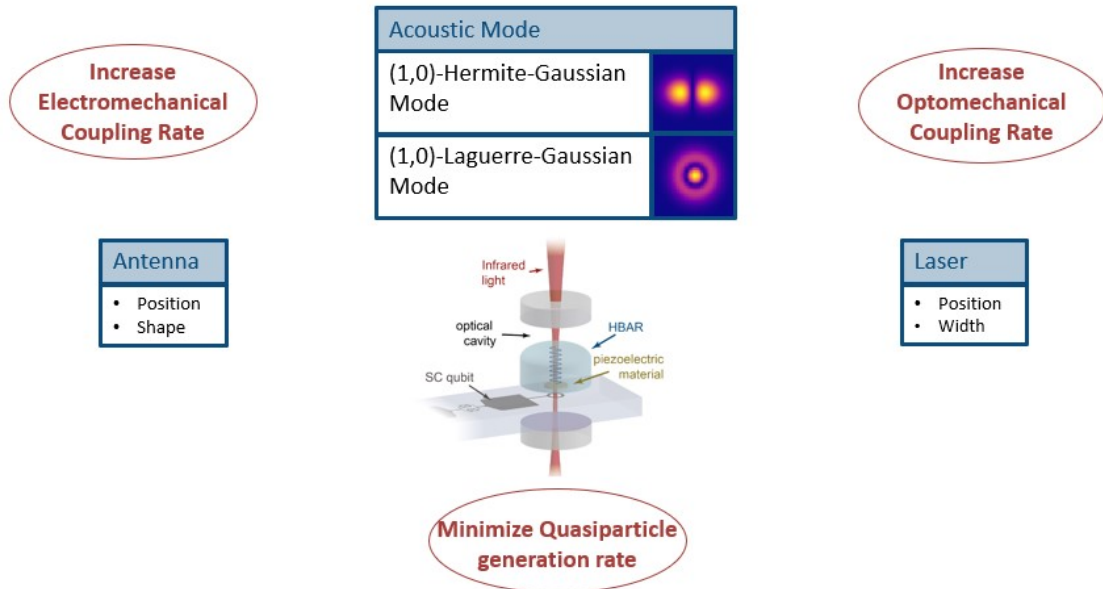

Figure 1.1.: Overview of transduction problem using acoustic HBAR modes for mediating quantum states between the microwave and the optical quantum states.

2

Background

In this section we recall the physical background of our quantum transduction experiment. We will start by explaining the principles of acoustic wave propagation and how acoustic waves can form standing modes. We will then explain how these acoustic modes can couple optomechanically and electromechanically to other quantum systems. Finally, we will explain the formation of quasiparticles inside a superconductor and discuss in what way quasiparticles play a role in our quantum transduction experiment.

2.1. Acoustic Modes

The formation of standing acoustic waves is a key feature of our quantum transduction experiment. To get a better understanding of it, we will work out the basics of acoustic waves in solids in the following chapter.

2.1.1. Solid Mechanics

Before we can start to understand the propagation of acoustic waves, we need to know the basic concepts of stress and strain. We will briefly introduce these concepts here.
We consider two neighbouring points M and N inside a three-dimensional solid, which are displaced by external forces. This displacement happens not necessarily in the same direction for both points. We can thus define a displacement vector for point M:

$$\vec{u}(\vec{x}) = \vec{x'} - \vec{x} \tag{2.1}$$

where $\vec{x}$ with coordinates x_i is the position vector of the point before the displacement and $\vec{x}'$ with coordinates $x_i' = x_i + u_i$ is the position vector after the displacement. The second point N has its initial position at $\vec{x} + \mathrm{d}\vec{x}$ with coordinates $x_i + \mathrm{d}x_i$. Its displacement is defined accordingly:

$$\vec{u}(\vec{x} + \mathrm{d}\vec{x}) = \vec{u}(\vec{x}) + \mathrm{d}\vec{u} \tag{2.2}$$

where we defined $\mathrm{d}\vec{u} = \frac{\partial \vec{u}}{\partial x}\mathrm{d}x + \frac{\partial \vec{u}}{\partial y}\mathrm{d}y + \frac{\partial \vec{u}}{\partial z}\mathrm{d}z$. The gradient of displacement $\frac{\partial u_i}{\partial x_j}$ is a second rank tensor and can be split up into a symmetric and an antisymmetric part:

$$\frac{\partial u_i}{\partial x_j} = \frac{1}{2}\left(\frac{\partial u_i}{\partial x_j} + \frac{\partial u_j}{\partial x_i}\right) + \frac{1}{2}\left(\frac{\partial u_i}{\partial x_j} - \frac{\partial u_j}{\partial x_i}\right) = S_{ij} + \Omega_{ij} \tag{2.3}$$

2. Background

The antisymmetric part Ω_{ij} describes any overall movement such as translations or rotations, whereas the symmetric part S_{ij} describes deformations within the medium and is defined as the second rank tensor strain:

$$S_{ij} = \frac{1}{2}\left(\frac{\partial u_i}{\partial x_j} + \frac{\partial u_j}{\partial x_i}\right) \tag{2.4}$$

Hence, strain is a measure for the deformation inside a medium.

Mechanical contact at the surface or inside the volume and applied fields can lead to external forces on a solid. The force inside a solid per unit area $\mathrm{d}\vec{F}/\mathrm{d}s$ is called mechanical traction $\vec{T}$. Mechanical traction is not necessarily perpendicular to the surface s on which we define it. Yet we can define a unit vector $\vec{l}$ normal to the surface, which we can relate to the mechanical traction as follows:

$$\vec{T}(\vec{l}) = T_{ik}\vec{l} \tag{2.5}$$

T_{ik} is what we then call the stress tensor.

The relation between the stress and the strain can be expressed in a Taylor expansion:

$$T_{ij}(S_{kl}) = T_{ij}(0) + \left(\frac{\partial T_{ij}}{\partial S_{kl}}\right)_{S_{kl}=0} S_{kl} + \frac{1}{2}\left(\frac{\partial^2 T_{ij}}{\partial S_{kl}\partial S_{mn}}\right)_{S_{kl}=S_{mn}=0} S_{kl}S_{mn} + ...$$

It has been shown experimentally that for small deformations we can omit higher order terms. We assume here, that there are no external forces acting on the surface of the solid ($T_{ij}(0) = 0$), such that we obtain Hook's law:

$$T_{ij} = c_{ijkl}S_{kl} \tag{2.6}$$

where we define $c_{ijkl} = \left(\frac{\partial T_{ij}}{\partial S_{kl}}\right)_{S_{kl}=0}$ to be components of the stiffness tensor.

Once we have defined the strain and the stress, we can take a look at the change of internal energy U per unit volume:

$$\mathrm{d}U = \delta w + \delta Q \tag{2.7}$$

where δQ is the heat gained per unit volume and $\delta w = T_{ij}\mathrm{d}S_{ij}$ is the change of elastic potential energy per unit volume. Using Hook's law we derived above, we get the change of elastic potential energy:

$$\begin{aligned}
\delta w &= T_{ij}\mathrm{d}S_{ij} \\
&= c_{ijkl}S_{kl}\mathrm{d}S_{ij} \\
&= \frac{1}{2}\left(c_{ijkl}S_{kl}\mathrm{d}S_{ij} + c_{ijkl}S_{ij}\mathrm{d}S_{kl}\right) \\
&= \frac{1}{2}c_{ijkl}d(S_{ij}S_{kl})
\end{aligned}$$

4

Hence we obtain the elastic potential energy per unit volume e_p as a quadratic function of the strain [12]:

$$e_p = \frac{1}{2}c_{ijkl}S_{ij}S_{kl}. \tag{2.8}$$

2.1.2. Helmholtz Equation and Orthogonal Waves

As we have now defined internal stresses inside a solid T_{ij}, we can use this definition to write down the equation of motion:

$$\rho\frac{\partial^2 u_i}{\partial t^2} = \frac{\partial T_{ij}}{\partial x_j} \tag{2.9}$$

where ρ is the material density. We have again assumed here, that there are no external forces acting on the surface of the solid. Rewriting Hooke's law (2.6) in terms of displacement:

$$T_{ij} = \frac{1}{2}c_{ijkl}\frac{\partial u_k}{\partial x_l} + \frac{1}{2}c_{ijkl}\frac{\partial u_l}{\partial x_x} = c_{ijkl}\frac{\partial u_l}{\partial x_k} \tag{2.10}$$

where we used the fact, that $c_{ijkl} = c_{ijlk}$, which made the two factors in the summation equal. We can then use this in the equation of motion:

$$\rho\frac{\partial^2 u_i}{\partial t^2} = c_{ijkl}\frac{\partial^2 u_l}{\partial x_j \partial x_k} \tag{2.11}$$

which is the wave equation in solids [12].

Next, looking for solutions of this wave equation, we consider paraxial waves: A paraxial wave vector is assumed to make small angles with the acoustic axis which, analogous to the optical axis, is the general propagation direction of the acoustic wave. To construct paraxial waves we take a plane wave and modulate it with a slowly varying complex envelope a:

$$u(x, y, z) = a(x, y) \exp(-ik_L z) \tag{2.12}$$

The transversal envelope $a(x, y)$ must satisfy the paraxial Helmholtz equation:

$$\nabla_T^2 a(x, y) + k_T^2 a(x, y) = 0 \tag{2.13}$$

where $\nabla_T^2 = \partial^2/\partial x^2 + \partial^2/\partial y^2$ is the transverse Laplace operator and k_T the transversal wave vector. We have made here the assumption that the material is isotropic in the transversal directions. This is true for longitudinal waves propagating along the c-axis of sapphire.

We consider two orthogonal sets of functions that solve this equation: HG functions and LG functions. You can see their intensity distribution in Figure 2.1 and we will later encounter these distributions when we simulate the acoustic modes inside the acoustic

resonator.

If $u(x, y, z)$ forms a standing mode in the resonator, its phase front has the same shape
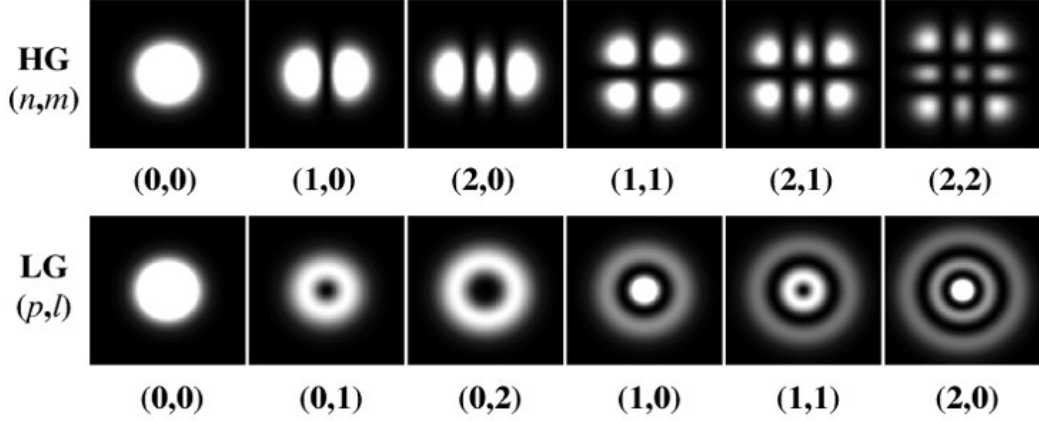
Figure 2.1.: Intensity distribution of LG and HG modes [13].

as the surface on which it gets reflected and the longitudinal wavevector k_L is fixed by [14]:

$$k_L = \frac{2\pi m}{L_{\mathrm{ac}}} \tag{2.14}$$

where L_{ac} is the length of the acoustic resonator.

2.2. Optomechanical Coupling

To efficiently transduce the phonon quantum state into a optical quantum state and vice versa we want to enhance coupling between the phonon and the optical mode. This coupling mechanism is based on Brillouin scattering. In the following section, we will first explain the general optomechanical Hamiltonian and then focus on the Brillouin-like interaction in more detail [15].

2.2.1. Optomechanical Coupling Rate

Optomechanical systems couple mechanical motion to cavity radiation fields. The fundamental mechanism that creates this coupling is the momentum transfer between the phonons of the mechanical motion and the photons of the radiation field. Momentum transfer from photons to phonons works trough radiation pressure. One of the simplest forms of radiation pressure is the momentum transfer caused by the reflection inside a Fabry-Pérot cavity. In our system, however, the radiation pressure mechanism is slightly more complex.

The radiation pressure mechanism in our system uses the electrostrictive force: The photon field displaces positive ions inside the crystal in direction of the electric field and negative ions in the opposite direction. The displacement results in an overall strain in the crystal, namely our phonon mode. The strain on the other hand modifies the medium's refractive index, creating an index grating. This grating scatters the photon into another mode at a slightly different frequency. This type of scattering is called stimulated Brillouin-scattering and accordingly we call the resulting optomechanical coupling Brillouin-like coupling.

As we have seen in equation 2.12, we can describe the acoustic mode as the product of an oscillation along the z-axis and a complex envelop in the x-y plane $S_0(x, y)$.

$$S(x, y, z) = s \cdot S_0(x, y) \cdot \sin(k_{\mathrm{ac}} z) \tag{2.15}$$

k_{ac} is the wavevector of the acoustic wave and s is here the normalization constant derived in section 2.2.3. Similarly, we can describe the electric field of the photon which is a mode of the optical cavity:

$$E(x, y, z) = e \cdot E_0(x, y) \cdot \sin(k_{\mathrm{op}} z) \tag{2.16}$$

where k_{op} is the wavevector of the optical cavity field and e is again the normalization constant further explained in section 2.2.3. We have introduced here the envelopes $S_0(x, y)$ and $E_0(x, y)$ in the x-y plane as this

Accordingly we can now consider the interaction Hamiltonian for the Brillouin-like optomechanical coupling:

$$H^{\mathrm{int}} = \frac{1}{2} \int_V \epsilon_0 \epsilon_r^2 E_{j+1}(x, y, z) E_j(x, y, z) p_{13} S(x, y, z) (\hat{a}_{j+1}^\dagger \hat{a}_j \hat{b} + \hat{a}_{j+1} \hat{a}_j^\dagger \hat{b}^\dagger) \mathrm{d}V \tag{2.17}$$

ϵ_r is the relative permittivity of the crystal and p_{13} is the photoelastic constant which couples the z-component of the strain S and the x-component of the photon fields E_s and E_p. The term $\hat{a}_{j+1}^\dagger \hat{a}_j \hat{b}$ represents the annihilation of an optical mode and a phonon mode to create a photon mode at the sum of their frequency and the other term $\hat{a}_{j+1} \hat{a}_j^\dagger \hat{b}^\dagger$ represents the creation of a photon and a phonon and the annihilation of a photon. Applying a strong control laser on the lower frequency leads to an effective beamsplitter Hamiltonian:

$$H^{\mathrm{int}} = -\hbar g_0^{\mathrm{om}} \sqrt{n_c} (\hat{a}_{j+1}^\dagger \hat{b} + \hat{a}_{j+1} \hat{b}^\dagger) \tag{2.18}$$

where g_0^{om} is the single photon optomechanical coupling rate:

$$g_0^{\mathrm{om}} = \frac{1}{2\hbar} \int_V \epsilon_0 \epsilon_r^2 E_{j+1}(x, y, z) E_j(x, y, z) p_{13} S(x, y, z) \mathrm{d}V \tag{2.19}$$

Thus applying a strong control laser on the lower frequency increases the optomechanical coupling strength by the square root of the intracavity photon number. How this

correlates with the input laser power is explained in section 2.2.6. Thus, ignoring the change in photon number of mode j, we note that we can either convert a photon into a phonon $(\hat{a}_{j+1}\hat{b}^{\dagger})$, which corresponds to Stokes scattering, or we can convert a phonon into a photon $(\hat{a}_{j+1}^{\dagger}\hat{b})$, which corresponds to anti-Stokes scattering [15].

2.2.2. Propertiers of Stimulated Brillouin Scattering

Phase Matching

Taking a deeper look into stimulated Brillouin scattering we can distinguish two types of it: Depending on the direction of the scattered photon, we call the process either forward or backward scattering. To achieve the high frequency acoustic phonon, which we need to get close to the energy or the qubit, we use backward scattering. The wave vector relation of backward scattering is shown in Figure 2.2.

The stimulated Brillouin scattering process must therefore fulfill the phase matching
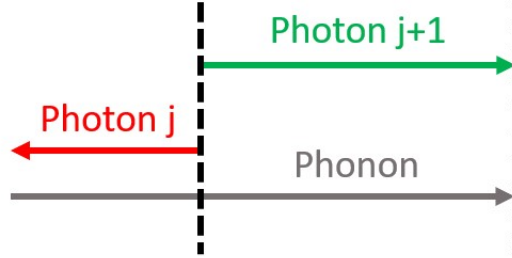
Figure 2.2.: Backward Stimulated Brillouin Scattering, where the pumped photon scatters into another photon and a phonon.

condition:

$$\vec{k}_{j+1} = \vec{k}_j + \vec{k}_{\mathrm{ac}} \tag{2.20}$$

where $\vec{k}_j$ is the wavevector of the photon at whose frequency we pump with the control laser, $\vec{k}_{j+1}$ is the wavevector of the photons at the higher frequency and $\vec{k}_{\mathrm{ac}}$ is the wavevector of the phonon mode [16].

Energy conservation

We have seen, that a Brillouin-like optomechanical process involves two optical modes: Due to energy conservation their frequency difference must be equal to the frequency of the acoustic mode Ω_{ac}:

$$\omega_{j+1} - \omega_j = \Omega_{\mathrm{ac}} \tag{2.21}$$

Here ω_{j+1} is the frequency of the higher energy photon and ω_j the frequency of the lower energy photon. Equation 2.21 can give us a deeper understanding of the electrostrictive force. The pump and the vacuum electric field of the scattered light generate a beating pattern which gives rise to the electrostrictive force. This force induces then a stress at the beating frequency which moves at the speed of sound [16, 17].

2.2.3. Normalization of Optical Modes

In order that we can later scale the total coupling strength with the laser power, we need to scale the amplitudes of the optical fields to the energy of a single photon. We do this by integrating the energy density over the volume of the optical cavity, which must then give us the energy of a single photon [15]:

$$\int_V \epsilon_r(x,y,z) \cdot |E(x,y,z)|^2 dV = \hbar\omega_0 \tag{2.22}$$

where

$$E(x,y,z) = a \cdot E_0(x,y) \cdot \sin(kz) \tag{2.23}$$

can describe either of the two photon modes. As we use a Gaussian laser beam to excite the cavity, the envelope E_0 for both photon modes will be Gaussian shaped but not yet normalized. By substituting this field into the normalization condition above we find a :

$$a = \sqrt{\frac{2\hbar\omega_0}{\epsilon_0 A_{\mathrm{op}}} \cdot \frac{1}{L_{\mathrm{ac}}(\epsilon_c - 1) + L_{\mathrm{op}}}} \tag{2.24}$$

where

$$A_{\mathrm{op}} = \int_{-\infty}^{\infty} \int_{-\infty}^{\infty} E_0(x,y)^2 dx dy \tag{2.25}$$

is the transversal optical mode area. L_{ac} and L_{op} are the physical length of the acoustic and the optical cavity. The whole calculation can be found in Appendix A.2.

2.2.4. Normalization of the Acoustic Mode

Similar to the normalization of optical modes above - since we only couple to a single acoustic mode at a time - we also need a normalization that accounts for the energy of a single phonon. We again integrate the energy density over the whole volume and set it equal to the energy of a single phonon [15]:

$$\int_V c_{33} \cdot |S(x,y,z)|^2 dV = \hbar\omega_{\mathrm{ac}} \tag{2.26}$$

where

$$S(x, y, z) = s \cdot S_0(x, y) \cdot \sin(kz) \tag{2.27}$$

is the strain field of the acoustic mode. Here the envelope S_0 is what we get out of the simulation and this is then not yet normalized. We can find the normalization constant s by substituting this expression into the normalization condition above:

$$s = \sqrt{\frac{2\hbar\omega_{\mathrm{ac}}L_{\mathrm{ac}}}{c_{33}A_{\mathrm{ac}}}} \tag{2.28}$$

where

$$A_{\mathrm{ac}} = \int_{-\infty}^{\infty}\int_{-\infty}^{\infty} S_0(x, y)^2 dx dy \tag{2.29}$$

is the transversal acoustic mode area. The derivation can be found in Appendix A.1

2.2.5. Crystal Position dependence

When aiming for maximal optomechancial coupling strength, we must also consider where within the optical cavity it is best to place the crystal. Earlier we saw that in backward-stimulated Brillouin scattering, the acoustic wave oscillates at the difference of the two optical frequencies. However, for stable acoustic modes to build up, it is also important to ensure that the acoustic wave satisfies boundary conditions at the crystal surfaces. This can be achieved by properly positioning the crystal within the optical cavity.

For calculating the optimal crystal position, we will take a look at equation 2.19. We insert the product form of the acoustic and the optical modes (equations 2.15 and 2.16) and by doing so we decompose the integral into an integration over the transversal plane and an integration along the z-axis. To determine the influence of the crystal position we only need to look at the integral along the z-axis. We then define the distance from the left mirror to the crystal facet as d and adjust the phases of the oscillations in the integral of equation 2.19 accordingly:

$$
\begin{aligned}
g_0^{\mathrm{om}} \propto & \int_d^{d+L_{\mathrm{ac}}} \sin\left(k'_{j+1}(z-d+\frac{d}{n})\right) \sin\left(k'_j(z-d+\frac{d}{n})\right) \sin(k_{\mathrm{ac}}(z-d))dz \\
= & \int_d^{d+L_{\mathrm{ac}}} \frac{1}{4}\left[-\sin\left((z-d)(-2k'_j)+\frac{d}{n}(k'_{j+1}-k'_j)\right)+\sin\left(\frac{d}{n}k_{\mathrm{ac}}\right)\right. \\
& +\sin\left(-(z-d)(2k'_{j+1})+\frac{d}{n}(k'_{j+1}-k'_j)\right) \\
& \left.+\sin\left((z-d)2k_{\mathrm{ac}}+\frac{d}{n}k_{\mathrm{ac}}\right)\right]dz \\
= & \frac{1}{4}\left[-\frac{1}{2k'_j}\left(\cos\left(\frac{d}{n}(k'_{j+1}-k'_j)-2k_jL_{\mathrm{ac}}\right)-\cos\left(\frac{d}{n}(k_{j+1}-k_j)\right)\right)\right. \\
& +L_{\mathrm{ac}}\sin\left(\frac{d}{n}k_{\mathrm{ac}}\right) \\
& +\frac{1}{2k'_{j+1}}\left(\cos\left(\frac{d}{n}(k'_{j+1}-k'_j)-2k_{j+1}L_{\mathrm{ac}}\right)-\cos\left(\frac{d}{n}(k_{j+1}-k_j)\right)\right) \\
& \left.+\frac{1}{2k'_j}\left(\cos\left(2L_{\mathrm{ac}}k_{\mathrm{ac}}+\frac{d}{n}k_{\mathrm{ac}}\right)-\cos\left(\frac{d}{n}k_{\mathrm{ac}}\right)\right)\right] \\
\approx & \frac{L_{\mathrm{ac}}}{4}\sin\left(\frac{d}{n}k_{\mathrm{ac}}\right)
\end{aligned}
$$

Here we have applied the sine multiplication rule [i] and the phase matching condition (equation 2.20) in the first step and in the second step we compared the amplitudes: The wavelengths and therefore the inverse optical wave vectors are much smaller than the acoustic crystal length. Thus all terms except the one with amplitude $\frac{L_{\mathrm{ac}}}{4}$ are negligible.

---

[i] $\sin(A)\sin(B)\sin(C) = \frac{1}{4}\left[-\sin(\text{A-B-C})+\sin(\text{A+B-C})+\sin(\text{A-B+C})-\sin(\text{A+B+C})\right]$

Thus, we can maximize the integral along the z-axis if we position our crystal at:

$$d = \frac{\pi n}{2 k_{\text{ac}}}$$

For a setup using CaF_2 as crystal, the optimal position is around 0.2 μm apart from a mirror while the coupling goes to zero as the crystal is positioned at the mirror itself or 0.4 μm apart. In practice, however, it is challenging to position the crystal exactly [15].

2.2.6. Laser Power Requirements

To this point we have only talked about the optomechanical coupling between a single photon and the acoustic mode. Thus, by shining the laser on the optical cavity, not only a single photon ends up in the cavity mode at ω_j, but multiple of them. The optomechanical coupling rate g^{om} scales with the number of intra-cavity photons n_c:

$$g^{\text{om}} = \sqrt{n_c} \cdot g_0^{\text{om}} \tag{2.30}$$

The number of photons that end up in the cavity is determined by the input laser power P_{in}:

$$n_c = \frac{1}{\kappa_c} \frac{P_{\text{in}}}{\hbar \omega_j} \tag{2.31}$$

where we have assumed that we are on resonance and that the cavity is symmetric and has no internal losses. The latter allows us to assume that the optical decay rate κ is solely determined by the coupling at the mirrors κ_c, which means $\kappa = 2\kappa_c$. κ_c can be estimated using the mirror reflectivity R and the optical path length of the cavity l_{op}: $\kappa_c = \frac{c}{2l_{\text{op}}}(1-R)$.
A standard way to compare the coupling rate and loss rates in an optomechanical system is the cooperativity C. Regarding microwave to optical transduction, we aim to achieve a cooperativity C greater than one:

$$C = \frac{4(g^{\text{om}})^2}{\kappa \gamma} \geq 1 \tag{2.32}$$

A cooperativity greater than one is generally needed for efficiently transducing quantum information [18]. For this reason we set the input laser power to a strength that allows us to work in a regime where $C > 1$ [19–21]:

$$P_{\text{in}} \geq \hbar \omega_j \frac{\kappa_c^2 \gamma}{2 g_0^{\text{om2}}} \tag{2.33}$$

2.3. Electromechanical Coupling

The transduction process from the qubit state to the phonon state happens via piezo-electric coupling. To understand the mechanism of piezoelectric coupling, we first look at piezoelectricity in general and then we discuss what the piezoelectric coupling strength depends on.

2.3.1. Piezoelectricity

As the word piezoelectricity comes from the Greek, it means "electricity through pressure". Exerting a pressure on a material can deform the internal crystal structure. This can separate the positive and negative charges inside the crystal thus forming little electrical dipoles and polarizing the material. This polarization generates an electric field and can be used in such a way to transform the mechanical energy from the deformation into electrical energy.

This process also works in the reverse direction: Applying an electric field separates positive and negative charges inside a crystal. This leads to a deformation within our material. The part of strain, which is produced by the piezoelectric effect, S^p, is then related to the electric field $\vec{E}$ via the piezoelectric strain tensor d:

$$S_i^p = d_{mi}E_m \tag{2.34}$$

So the overall strain in the crystal becomes:

$$S_i = s_{ij}T_j + d_{mi}E_m \tag{2.35}$$

where we used the Voigt notation, $i, j = 1$ to 6, $m = 1$ to 3 and s_{ij} are the elements of the inverse of the stiffness tensor c_{ij} [22].

2.3.2. Electromechanical Coupling Strength

Now, to calculate the piezoelectric coupling strength g^{em}, we take a look at the interaction Hamiltonian of the strain field S and the electric field from the antenna E^{ant} [19]:

$$H_{\text{int}} = \int_V d \cdot c_E \cdot S(x, y, z) \cdot E^{\text{ant}}(x, y, z) \, (\hat{a}^\dagger \hat{b} + \hat{a}\hat{b}^\dagger) \mathrm{d}V \tag{2.36}$$

Where the term $\hat{a}^\dagger \hat{b}$ represents the annihilation of a phonon and the creation of a microwave photon and the term $\hat{a}\hat{b}^\dagger$ represents the creation of a phonon and the annihilation of a microwave photon. We assume that the electric field stays constant over the small length of the piezoelectric layer in our sample ($E(x, y, z) = E(x, y)$) and we again use the oscillating strain field from equation 2.15. This way we obtain the electromechanical

coupling strength:

$$g^{\text{em}} = \frac{1}{\hbar} \cdot \left(\int_{-\infty}^{\infty} \int_{-\infty}^{\infty} d \cdot c_E \cdot s \cdot S_{0zz}(x,y) \cdot E_z^{\text{ant}}(x,y) \, \mathrm{d}y \, \mathrm{d}x \right) \cdot \left(\int_0^{t_p} \sin(kz) \, \mathrm{d}z \right) \quad (2.37)$$

where t_p is the thickness of the piezo layer. We assumed here, that the only non-zero piezo tensor component is d_33.From this equation, you can see that if the thickness of the piezoelectric layer t_p is half an acoustic wavelength, the second term is maximized. We should therefore aim for a t_p of half an acoustic wavelength, which is, in the case of LiNbO$_3$, around 0.27 μm.

2.4. Quasiparticle Generation

A common non-equilibrium effect in superconductors is the formation of quasiparticles [23]. Quasiparticles are elementary excitations, which are created when Cooper pairs in superconductors are split by sufficient energy. The energy needed for this is:

$$\epsilon \approx 1.65\Delta \quad (2.38)$$

where Δ is the superconducting gap (for aluminum $\Delta_{\text{Al}} = 0.18$ meV [24]).
The formation of quasiparticles at low temperatures is exponentially suppressed [25]. For superconducting aluminium at temperatures lower than 20 mK only one quasiparticle in the volume of the Earth should exist [24]. Yet, a significant background of quasiparticles has been observed in other experiments working at low temperatures [11, 26]. In our experiment we additionally shine infrared light into the system, which provides even more energy to create a significant amount of quasiparticles [27, 28].
The effects of quasiparticles in our system are various. To better understand them, we define the normalized quasiparticle density $x_{\text{qp}} = n_{\text{qp}}/n_{\text{cp}}$, where n_{qp} is the quasiparticle density and n_{cp} is the Cooper-pair density. If the normalized quasiparticle density is greater than one, superconductivity breaks down. But already at smaller densities x_{qp}, quasiparticles cause relaxation of transmon qubits. The energy relaxation rate of a transmon due to quasiparticles is:

$$\Gamma_{\text{qp}} = \sqrt{\frac{2\omega_q \Delta}{\pi^2 \hbar}} x_{\text{qp}} \quad (2.39)$$

where ω_q is the qubit frequency [11].
The motion of quasiparticles over our device is quite complex and not yet fully understood. But it is important to note here, that the quasiparticle density is defined locally. For example, if we have local superconductivity breaking, Cooper pairs from other areas can rebuild the superconductivity. Furthermore, quasiparticles closer to the transmon affect the relaxation rate more than those at the antenna.
To be able to estimate the quasiparticles in our system, we therefore need some sim-

plifications: First we ignore all kind of quasiparticle motion. Then we only consider quasiparticles generated by the IR laser light and neglect all other sources of quasiparticles. The intensity of the Gaussian laser beam is

$$I(x, y, z) = \frac{2P_0}{\pi w_0^2} \left(\frac{w_0}{w(z)} \right)^2 \exp\left(\frac{-2(x^2 + y^2)}{w(z)^2} \right) \tag{2.40}$$

where P_0 is the total power of the laser beam, w_0 is the waist radius at the focus and $w(z)$ the waist radius at a distance z from the focus. If we divide the local intensity by the energy needed to form a quasiparticle ϵ, we get the local quasiparticle generation rate:

$$g_s(x, y, z) = \frac{\partial n_{\mathrm{qp}}(x, y, z, t)}{\partial t} = \frac{I(x, y, z)}{\epsilon} \tag{2.41}$$

We can thus estimate the local QP density generated by a laser pulse of duration τ_l:

$$n_{\mathrm{qp}}(x, y, z) = \frac{I(x, y, z)}{\epsilon} \cdot \tau_l \tag{2.42}$$

Martina Solini has calculated in her thesis [28] at which generation rate the superconductivity locally breaks. This happens for $g_s^{th} = 5.5 \cdot 10^6 \ \mu\mathrm{m}^{-2}\mu\mathrm{s}^{-1}$. We will later use this value to compare different antenna shapes and to look at what radius around the laser the generation rate drops below this value. A more complete discussion of the problems caused by quasiparticles can be found in Martina Solini's semester thesis [28].

Device Design

Figure 3.1 shows the setup of the quantum transduction experiment using acoustic bulk modes. On a sapphire wafer is a superconducting qubit connected to an antenna. The antenna emits the electric field of the superconducting qubit trough the piezoelectric material. The piezoelectric material is deposited on a Calcium Fluoride (CaF_2) crystal - the high-overtone bulk acoustic wave resonator (HBAR, Figure 3.2). Around the HBAR is an optical cavity with a flat and a concave mirror placed. The flat mirror is near the HBAR and the concave mirror is on the other side of the sapphire wafer. An infrared laser shining into the optical cavity can excite standing optical modes there.
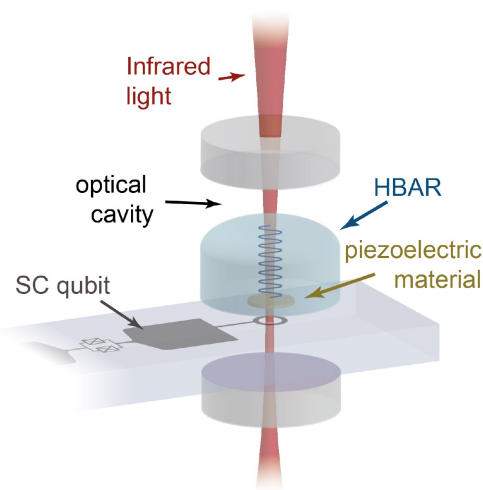

Figure 3.1.: Quantum transduction experimental setup

3.1. Bulk Acoustic Wave Resonator

To obtain confined modes in the HBAR, it is needed to introduce curvature in one of the two surfaces perpendicular to the propagation axis of the IR light. Up to this point, a spherical dome was usually etched out of one of the surfaces [29]. Measurements have shown that this dome is well described by the uppermost section of a sphere. This sphere can have radii between 5 and 60 mm, depending on the material and the fabrication process. The dome protrudes only about 1.2 μm from the rest of the surface. Hence, the

17

3. Device Design

angle between the crystal surface and the curvature of the dome is very small. In addition, the mode is localized only at the center of the dome. For this reason, the rest of the dome shape is not a determining factor for the shape of the mode.
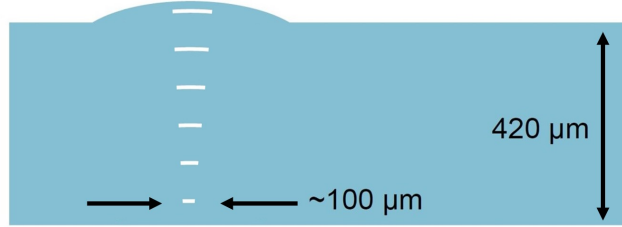

Figure 3.2.: HBAR with curved surface shape

Part of this work was to modify the shape of the curvature on the top to obtain differently shaped acoustic HBAR modes. Our goal was to obtain a mode consisting of two spatially separated parts. One part should be well overlapped with the modes of the optical cavity and the other with the electric field of the antenna from the superconducting qubit.

The electromechanical coupling between the electric field of the antenna and the acoustic mode requires a piezoelectric layer, which for maximum coupling should have the thickness of half a wavelength (as we have learned in Section 2.3). The layer is always on the side which is closer to the antenna. Whether it is also on the same side as the curvature shape, remains to be seen. This depends mainly on the fabrication process. In the scope of this work, the piezoelectric layer was always assumed to be on the side of the curvature.

For optimized electromechanical coupling, we also need to adjust the shape of the antenna. Yu Yang tested different shapes in his master's thesis [30]. In this work, we will limit ourselves to a ring-shaped and a circular antenna.

Choosing the right materials is also an essential part in optimizing coupling rates. So far, the HBAR was made of sapphire and the piezoelectric layer was aluminum nitride. We hope, however, that if we make the HBAR from calcium fluoride (CaF_2), we will be able to benefit from the higher photoelastic constant. Furthermore, we hope that if we use lithium niobate ($LiNbO_3$) as the piezoelectric material, we can take advantage of the better piezoelectric constant and smaller microwave losses. We will therefore use the properties of CaF_2 and $LiNbO_3$ for the analyses in this work.

Simulation of acoustic modes

As we have seen, the acoustic mode is the link between the microwave signal and the optical signal in our implementation of quantum transduction. Hence, to get an accurate estimate of the transduction parameters, it is important to understand the shape and size of the acoustic mode precisely. In order to do so, we simulate the acoustic mode in a Python script - the BeamProp simulation. In the following section we will describe the details of the simulation procedure.

Before we start the simulation process, it is necessary to define various key parameters. The first thing to set is the length of the crystal and the size of the plane on which the transversal mode exists. In order to limit the mode along the transversal plane, we then define an absorption radius, outside of which the intensity of the mode is gradually set to zero. We can then specify the sound velocity and Brillouin frequency of the crystal, which allow us to determine the longitudinal mode number via the crystal length.

In order to obtain stable modes in a crystal, at least one surface must be curved accordingly. Adjusting the shape of the crystal surface enables us to modify the mode shape. For example, we get LG shaped modes if we have a dome-shaped surface on one side as you can see in Figure 4.1a. And by changing the size of this dome we can modify the the transversal size of the mode.

When we set the surface of the crystal, we also need to account for the piezoelectric layer. We do this by changing the thickness of the surface according to the time it takes for the sound to travel trough the piezoelectric layer. It is important to note here, that by doing so, we neglect all possible reflections from the interface of the crystal and the piezoelectric layer.

As we will later find the modes by propagating the acoustic field inside the crystal back and forth, it is important to choose the shape of the initial field carefully. The symmetry of this initial shape will be reflected in the symmetry of the modes that we find in our simulation. For example, we will only find the centrally symmetric Laguerre Gaussian modes if our initial field was also centrally symmetric (see Figure 4.1b).

Once all initial parameters have been set, we can propagate the acoustic field back and forth for a range of different acoustic frequencies. Propagating the field one round trip is done in the following way: Starting on one side of the crystal, we do a Fourier transformation of the initial field and propagate it to the other side. There we Fourier transform the field back to the real space and we account then for the reflection by shifting the phase accordingly. Doing another Fourier transformation, we then propagate back and we do another Fourier transformation before we reflect at the other surface by again shifting the phase. For the next round of propagation we take the acoustic field we ob-

tained from the previous round trip. After each round trip the field is added up with the fields obtained from previous round trips. This way fields can interfere constructively or destructively. After a certain number of round trips we calculate the magnitude square of the field to get a local intensity and integrate over the transversal plane which gives us the total intensity. Calculating this intensity for different frequencies within the acoustic free spectral range we get a spectrum with peaks at frequencies with constructive interference, which are the acoustic modes in the crystal (see Figure 4.1c).

In a next step, we want to have a more detailed picture of the shape of the modes. To achieve this, we use the same initial field as before and let it again propagate back and fourth at the at the peak frequencies. For each round trip we start again by using the field obtained from the previous round trip. By doing more round trips than before and restarting with the found mode profile as initial field, we gain a more detailed picture of the mode shape in the transversal plane. Figure 4.1d shows an example of such a mode. This transversal mode shape we will later use to do follow-up calculations.
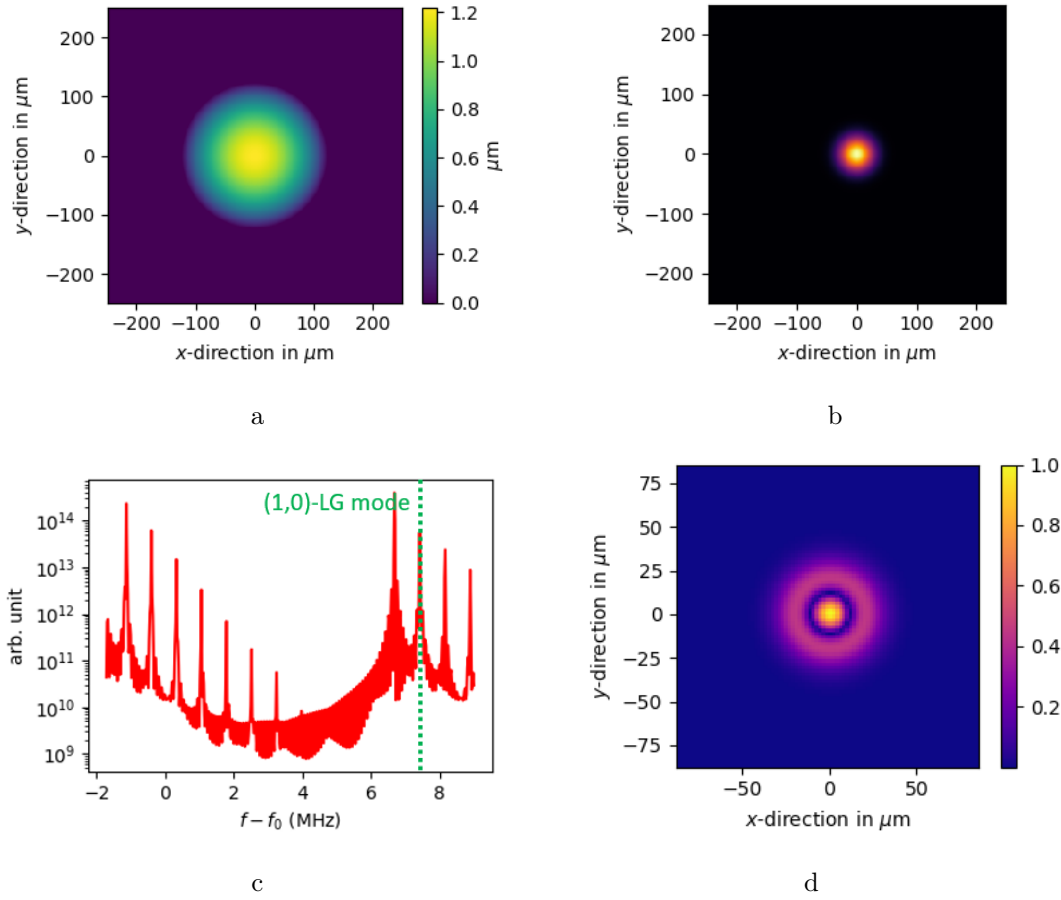
Figure 4.1.: **a)** Curved surface of crystal (dome protrudes flat HBAR surface), **b)** Centrally symmetric initial acoustic field strength that is used for the simulation of the spectrum **c)** and for the simulation of the various acoustic modes like **d)**. **c)** Acoustic mode spectrum from added up fields, where two sets of modes belonging to two different free spectral ranges can be observed (as the frequencies range over 1.25 of a free spectral range) **d)** Transversal shape of the absolute value of the acoustic mode field inside crystal (here the (1,0)-LG mode)

Optimization Analysis for (1,0)-Hermite-Gaussian and (1,0)-Laguerre-Gaussian Mode

In the following analysis, we will compare the (1,0)-LG mode and the (1,0)-HG mode against each other. Both modes consist of two regions with opposite sign - our desired spatially separated parts which can couple individually electromechanically and optomechanically. Also, both mode shapes are mathematically well understood.

We chose to compare the (1,0)-LG and the (1,0)-HG modes for various reasons. On one hand is their appearance well understood. We can say with confidence, that all parts of the mode belong to one single mode and that we can excite the whole mode although spatially overlapping just with one part. On the other hand, the fabrication of their belonging surface curvature is well developed and understood. In earlier experiments, we always used the spherical dome shape and also a ellipsoid surface shape fabrication can be done similar to a spherical dome surface. In contrast, in the case of double dome modes, where two domes are spatially overlapping and their center are about 10 μm apart, more work would have to be invested into development of the fabrication procedure. As some quick testing has shown, the known fabrication procedure does not work here.

We have seen and understood the emergence of these two types of modes in various BeamProp simulations. For a simple dome we get LG modes if we start the BeamProp Simulation with a centered symmetric initial field. If the initial field is not centered or symmetric, we can excite HG modes. Transferring this concept to the real experiment, one will excite LG modes with a centered Gaussian laser beam and HG modes with a non-centered beam. For the ellipsoid surface shape, as we have a lack of central symmetry, we only get HG modes. But since the (1,0)-HG mode has a zero at the center, we obtain this mode solely by exciting the HBAR not centrally. The initial fields are shown in Figures 5.1b and 5.1c. We can note here that the different sizes of the initial fields do not affect the mode shape as long as they initial field has the same symmetry as the mode shape.

To provide a basis for a comparable situation, we decided to take the LG and HG modes of the same spherical dome. As we will see later, the size of the modes plays an important role and this way we can ensure that they have a comparable size. Figure 4.1a shows the surface we used to get the (1,0)-Hermite- and (1,0)-LG mode (Figures 5.1d and 5.1e) we will compare in the following chapter. In Section 5.4, we will, however, also discuss how

23

we can change the shape of the HG mode to further optimize our system.

It is important to note here, that the purpose of this analysis is not only to compare LG and HG modes but also to serve as a guide in case one wants to analyze other mode shapes in the future.
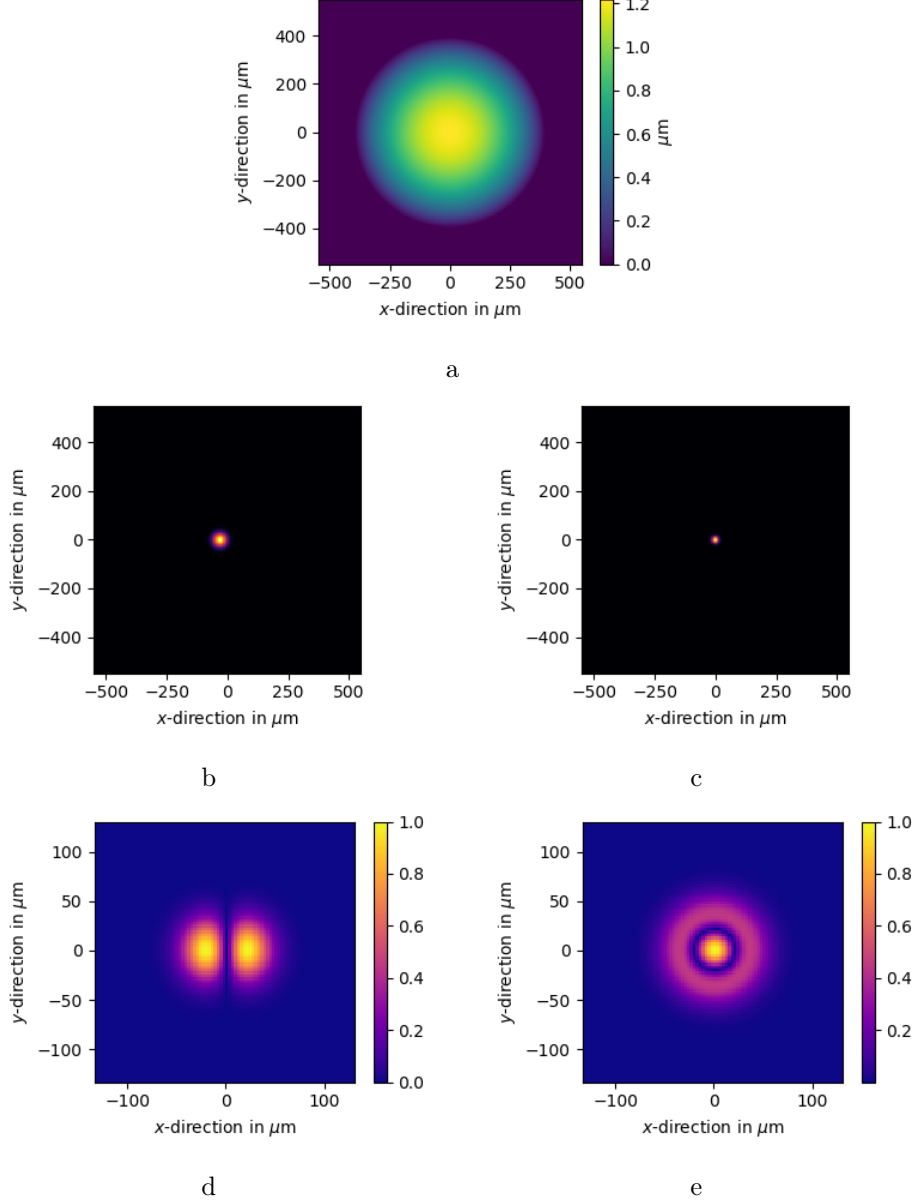

Figure 5.1.: **a)** Spherical HBAR surface, **b)** non centered initial field to obtain (1,0)-HG mode, **c)** centered initial field to obtain (1,0)-LG mode, **d)** (1,0)-HG mode and **e)** (1,0)-LG mode.

5.1. Electromechanical Coupling to (1,0)-Hermite-Gaussian and (1,0)-Laguerre-Gaussian Mode

The transduction process between the superconducting qubit and the phonon of the acoustic mode is determined by the electromechanical coupling strength. Thus, to enable fast operations between the two quantum states, the electromechanical coupling strength needs to be optimized. What is needed to achieve this and what we need to consider when doing so is treated in this section.

Equation 2.37 describes the electromechanical coupling strength g^{em} split into an integral along the z-axis and an integral over the transveral plane. Earlier we showed that the integral over the z-axis is maximized when we set the thickness of the piezoelectric layer to half an acoustic wavelength. Now, we will ask ourselves what it needs to optimize the integral over the xy plane.

For the optimization of the transversal integral we can adjust two points: If we first choose suitable materials, we have a high piezoelectric strain coefficient d and a high stiffness coefficient c_E. We believe that the piezoelectric Lithium Niobate can offer us this. If we then adjust the shape of the antenna and the acoustic mode, we can increase their overlap integral. Unlike you will see in the optomechanical case, the overlap in the electromechanical case gets maximized when the shape of the electric field and the shape of the acoustic mode are the most similar.

5.1.1. Antenna Size and Shape

To find antennas with a suitable electric field, Yu Yang simulated several electric fields from different antennas shapes using the software ANSYS. For the (1,0)-HG mode we selected circular antenna shapes that will overlap with one half of the mode and for the (1,0)-LG mode we selected ring antenna shapes that will overlap with the outer circle of the mode. In Figure 5.2 both modes with the according antennas and optical fields are shown. In the following section, we will now try to find the optimal sizes.

In Figure 5.3a we show the electromechanical coupling to the (1,0)-HG mode for differently sized antennas. For each calculation, the antenna was positioned such that the electromechanical coupling was the strongest. We observe that the coupling strength for antennas with radii between 22 and 32 um increases as the antenna becomes larger.

However, as the antenna gets larger, its edge gets closer to the position of the laser beam, which is at the other maximum of the acoustic mode. For a better understanding of this, Figure 5.3b shows the distance between the edge of the antenna and the center of the laser beam. This distance peaks at a radius of 26 μm and decreases thereafter. Hence, for the following analysis, we will focus on the antenna with a radius of 26 μm, which couples with a coupling strength of $g^{\text{em}} = 351 \cdot 2\pi$ kHz.
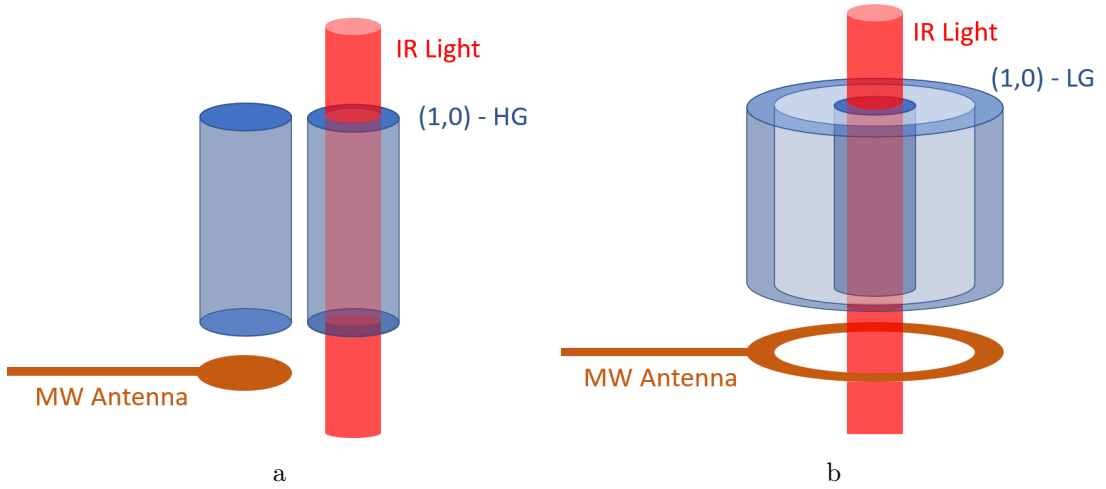
Figure 5.2.: **a)** (1,0)-HG mode couples with circular antenna and optical field. **b)** (1,0)-LG mode couples with ring antenna and optical field
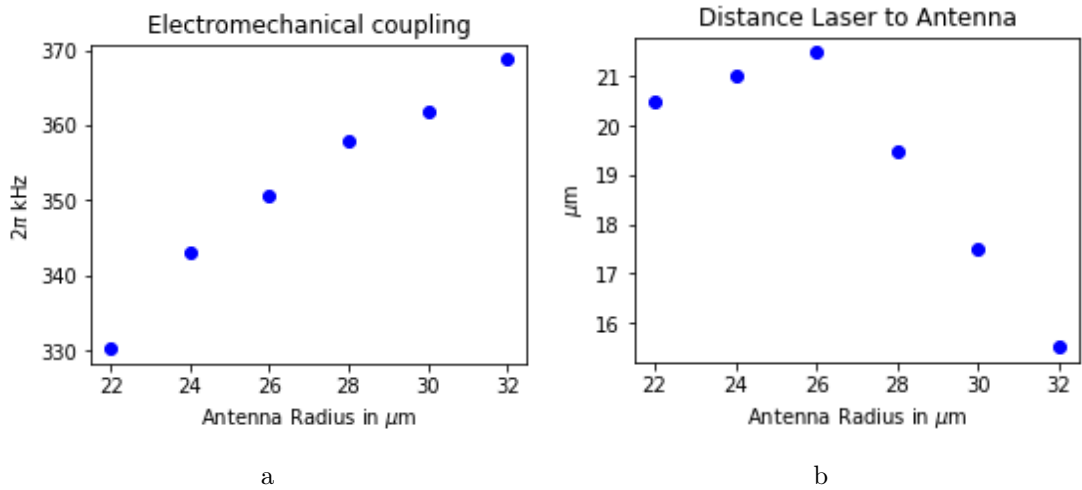

Figure 5.3.: **a)** Electromechanical coupling strength for different antenna radius, **b)** Distance from center of laser to the antenna edge.

Table 5.1 shows the electromechanical coupling from the (1,0)-LG mode to different ring antennas. The coupling between the (1,0)-LG mode and the ring antenna is stronger than the coupling between the (1,0)-HG mode and the circular antenna. The reason for this might be that the ring better matches the shape of the (1,0)-LG mode than the circle matches the shape of one side of the (1,0)-HG mode.

For choosing the optimal antenna shape one must consider three things: First, the coupling to the acoustic mode must be strong. Then, the antenna should not be too close to the laser, which is centered in the middle. And finally, the antenna surface must be

as small as possible, so that minimal laser power is absorbed. Ring 4 seems to be well suited for these criteria as we will discuss in more detail later.

	r_{inner} [μm]	r_{outer} [μm]	$g^{\text{em}}/2\pi$ [kHz]
1	40	60	1283
2	43	52	1163
3	45	50	1035
4	45	55	1143
5	77	88	248

Table 5.1.: Electromechanical coupling to different antennas

5.1.2. Electromechanical selectivity

The coupling strength to the selected acoustic mode is not the only determining factor for the transduction efficiency. It is in addition essential to prevent the antenna from coupling strongly to other acoustic modes. We can achieve this in two ways. First, by keeping the overlap of the other modes with the antenna small, we call this the spatial selectivity. Second, by separating the frequencies of the modes so that we excite only one mode with the frequency of the antenna field.

Figure 5.4 shows the spectra of the dome from Figure 5.1 which were obtained by the non-centered excitation (5.4a) and the centered excitation (5.4b). Thus, Figure 5.4a shows the spectrum when exciting the (1,0)-HG mode and Figure 5.4b shows the spectrum when exciting the (1,0)-LG mode. The frequency spacing in the spectrum when exciting the (1,0)-LG mode is twice as large as that of the spectrum when we excite the (1,0)-HG mode. Hence, we conclude that for the (1,0)-LG mode, we can better suppress the excitation of other modes and thus have better selectivity (provided that the coupling rate to unwanted modes is similar in both cases).
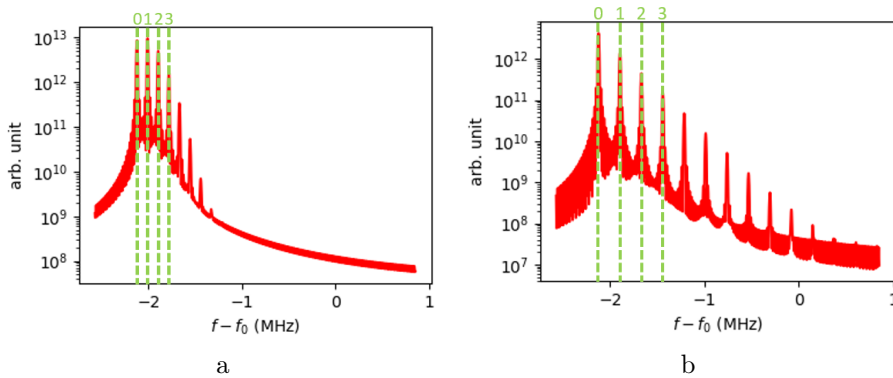

Figure 5.4.: a) Spectrum of non-central excited HBAR b) Spectrum of central excited HBAR

5.2. Optomechanical Coupling to (1,0)-Hermite-Gaussian and (1,0)-Laguerre-Gaussian Mode

To transduce a quantum state between the acoustic mode and an optical mode of the cavity, good optomechanical coupling is needed. In principle, the optomechanical coupling rate can be increased simply by adding more photons to the cavity - meaning increasing the power of the laser. But if we send more photons into the cavity, more photons end up on the antenna where they generate quasiparticles. So to keep the number of photons low but still increase the coupling rate, we need to optimize the single photon coupling rate g_0^{om}.

Several factors contribute to the single-photon coupling rate described in equation 2.19: The relative permittivity ϵ_r and the photoelastic constant p_{13} are determined by the material choice. As finding suitable materials is outside the scope of this work, we will not discuss it further. The overlap integral of the two photon modes and the acoustic mode is determined by the respective mode shape, which we would like to optimize here. We have already seen in section 2.2 that it is possible to split the overlap integral into an integral along the z-axis and an integral over the transversal plane. For maximizing the integral along the z-axis, it is essential to find the right crystal position. For maximizing the integral over the transversal plane, the situation is a littler more complex. While the overlap of two normalized functions gives a maximum when both functions are equal, we need to have a closer look at the situation with three normalized functions (see equation 5.2).

5.2.1. Overlap Integral of three normalized Gaussian functions

To gain an intuition on how three normalized functions must relate to each other in order to maximize their overlap integral, we consider 3 Gaussian distributions:

$$f_i(x) = \sqrt{\frac{2}{\pi W_i^2}} \cdot \exp\left(-\frac{x^2 + y^2}{W_i^2}\right) \tag{5.1}$$

In the experiment, the two optical modes will have the same width W_{op}, whereas the acoustic mode width W_{ac} can be different. Thus, the overlap integral gives

$$O = \sqrt{\frac{8}{\pi}} \cdot \frac{W_{\mathrm{ac}}}{2W_{\mathrm{ac}}^2 + W_{\mathrm{op}}} \tag{5.2}$$

The extensive calculation of the overlap integral can be found in Appendix A.3. Equation 5.2 is plotted in Figure 5.5. We observe that having a fixed optical width bigger than a certain value, we find a optimal width of the acoustic mode at $W_{\mathrm{ac}} = \sqrt{W_{\mathrm{op}}/2}$. But most importantly, there is no optimal optical waist size. Decreasing the optical waist size always improves the optomechanical coupling strength.
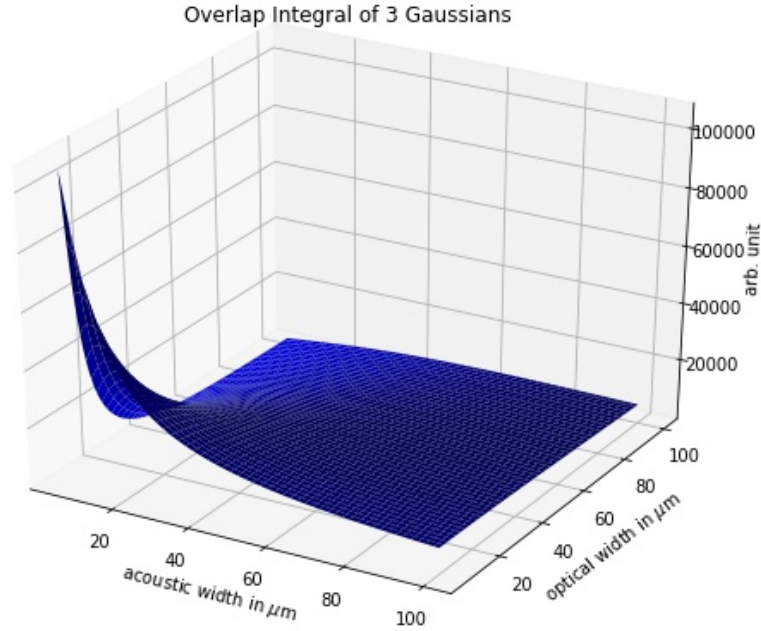
Figure 5.5.: Overlap of three Gaussians. Two modes have the same waist - the optical waist, which matches the laser waist, and the third mode, the acoustic mode, has a different waist.

5.2.2. Laser Width and Position

For the analysis here, we do not consider Gaussian-shaped acoustic modes but LG and HG modes which form higher order modes of the HBAR. Hence, the question arises how the behavior from Figure 5.5 can be applied to these modes. To figure this out, we take the HBAR modes described in Figure 5.1 and calculate the optomechanical coupling between them and two optical modes with varying waist sizes.

Figure 5.6 shows the coupling to the LG mode. The centers of the two optical modes and the LG mode thereby always coincide. We can again observe that for small waist sizes, the coupling becomes increasingly stronger and we can further observe that at an optical waist size of about 42 μm the coupling is weakest. Here the optical modes overlap with both parts of the (1,0)-LG mode with opposite signs, in such a way that the coupling almost disappears.

In Figure 5.7, we see the optomechanical coupling strength to the HG mode. In the case of HG mode, it is not immediately obvious where we must place the optical modes

to achieve the strongest coupling. For this reason, we vary not only the waist size but also the center of the optical modes. Again, we observe that for smaller optical modes the coupling strength increases. Moreover, we can see that for small optical modes, the strongest coupling arises, when placing the optical mode on the maximum of the acoustic mode. For larger optical modes the maximum then shifts away from the center, such that overlapping with the part of the mode of opposite sign is avoided.
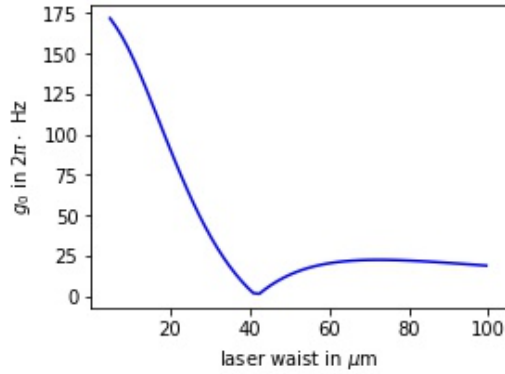

Figure 5.6.: Single photon optomechanical coupling rate between the (1,0)-LG mode shown in Figure 5.1e and optical modes with varying waist sizes.
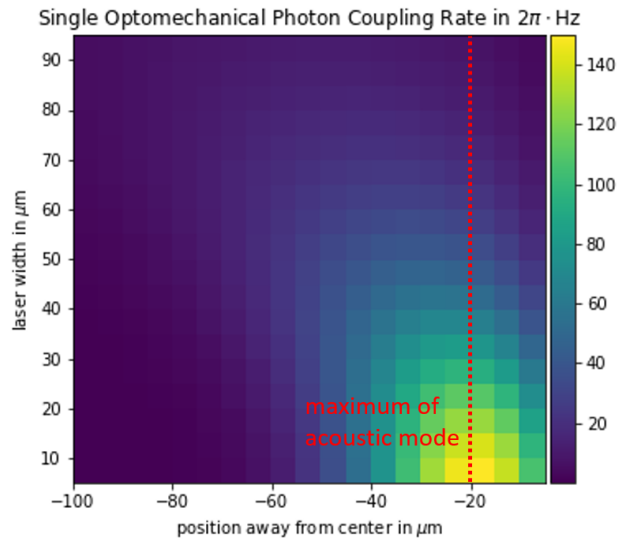
Figure 5.7.: Single photon optomechanical coupling rate between the (1,0)-HG mode shown in Figure 5.1d and optical modes with varying waist sizes and varying positions.

The above observations suggest us to use smaller optical modes to improve the optomechanical coupling strength. This can be achieved by reducing the size of the laser waist. In doing so, however, we are limited by the optical cavity setup.

A look at the optical laser setup allows us to estimate the smallest usable optical mode waist: We shine the laser through a hole of about 1.5 mm in diameter and focus the laser at some distance later, where the HBAR is located. This distance is fixed by the optical cavity length, which itself is determined by its free spectral range corresponding to the Brillouin frequency. If we reduce the waist size in the focus of a Gaussian laser beam, the waist size along the z-axis diverges stronger. That means we can reduce the size of our focused waist size only so much that the waist size 2 cm in front of it still fits through the hole. Calculations, which are in the Appendix A.6, suggest that this minimum waist size is approximately 20 μm.

To ensure that we can still assume a constant optical waist size over the length of the HBAR, we need to consider the Rayleigh length. The Rayleigh length is a measure for the length over which a Gaussian beam waist increases by a factor of $\sqrt{2}$. Going to smaller focused waist sizes, the Rayleigh length decreases and the beam diverges more strongly. At an optical wavelength λ_{op} of 1550 nm and a focused waist size of 20 μm, the Rayleigh length $z_R = \pi W_{\mathrm{op}}^2/\lambda_{\mathrm{op}}$ is approximately 1.62 mm. Comparing this to the length of the HBAR (l=0.42 mm), we can assume that the beam waist remains constant over the entire HBAR.

At the smallest possible laser waist $w_{\mathrm{op}} = 20$ μm, we can now compare the single-photon coupling rate. For the LG mode we set the laser in the center and get $g_0^{\mathrm{om}} = 92 \cdot 2\pi$ Hz. To get the rate of the HG mode, we set the laser to the maximum of the HG mode and get $g_0^{\mathrm{om}} = 98 \cdot 2\pi$ Hz. In terms of optomechanical coupling strength, both modes seem to perform equally well.

5.2.3. Optomechanical Selectivity

In the realization of quantum transduction it is not only important to increase the coupling between the selected modes but also to avoid coupling to other non-selected modes. For the optomechanical coupling this specially holds for the transduction of a optical quantum state to the acoustic quantum state. If the optical modes couple too much with other acoustic modes, the quantum state ends up in multiple acoustic modes and can not be transduced to the antenna properly.

The coupling is strongest to those modes which are closest in frequencies to the selected mode. For the (1,0)-LG mode this are the (0,0)- and the (2,0)-LG modes and analogously for the (1,0)-HG mode this is the (0,0)- and the (2,0)-HG mode [30].

Figure 5.8a shows the single-photon optomechanical coupling rate between the (0,0)-, the (1,0)- and the (2,0)-Hermite Gaussian mode. Figure 5.8b shows the coupling rate to the (1,0)-Hermite Gaussian mode divided by the sum of the coupling rates to the non-selected modes.

We can again observe the increase of coupling as we go smaller in laser waist. In addition, the ratio of coupling to the selected mode to coupling to non-selected modes also

increases. Regarding the (1,0)-Hermite Gaussian Mode, this implies that we can not only increase optomechanical coupling but also optomechanical selectivity if we reduce the laser waist.

We further observe that we can reach an optimal selective coupling to the (1,0)-Hermite Gaussian mode if we shine the laser onto the right position. As we shine the laser onto the maximum of the (1,0)-Hermite Gaussian mode, the coupling strength gets as big as the sum of the couplings to the (0,0)- and (2,0)-Hermite Gaussian modes.

Figure 5.9a shows the single photon coupling strength to the (0,0)-, (1,0)- and (2,0)-LG
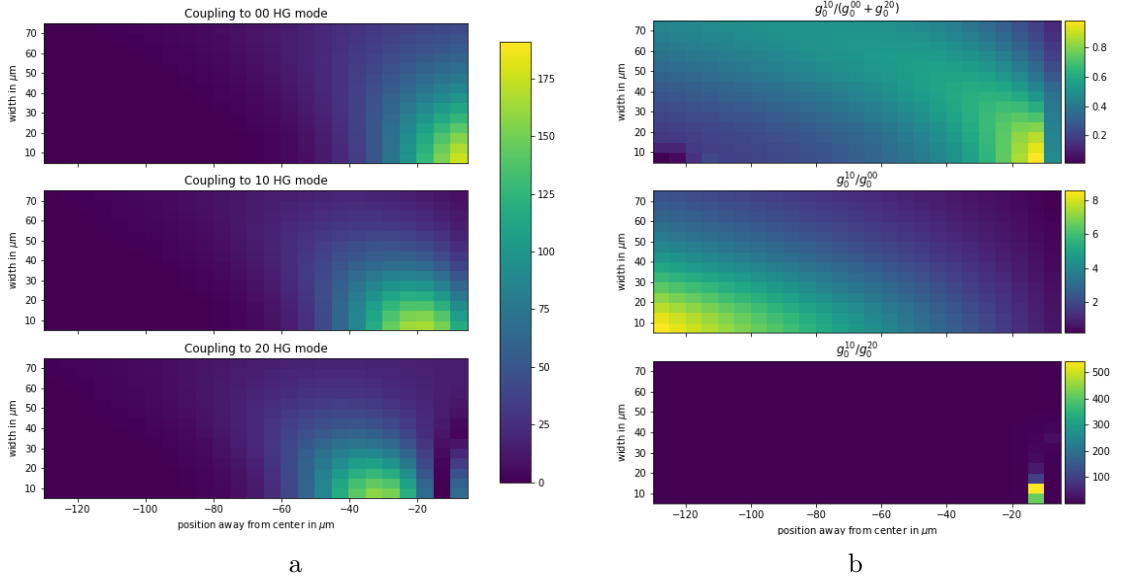
Figure 5.8.: **a)** Single photon optomechanical coupling rate to the (0,0)-, (1,0) and (2,0)-HG mode for different optical mode positions and waist sizes. **b)** Single photon optomechanical coupling rate to the (1,0)-HG mode divided by the sum of the coupling rates to the (0,0) and the (2,0) mode, divided only by the coupling rate to the (0,0) mode and divided only by the coupling rate to the (2,0) mode.

modes and Figure 5.9b shows the ratio of the coupling strength to the (1,0)-LG mode divided by the coupling strength to the non-selected modes. As with the HG modes, we see that not only the coupling strength improves for smaller waists, but also the optomechanical selectivity. For the LG modes, there are two optimal positions where the coupling to one mode becomes much larger compared to the coupling to the other modes. Yet, exciting the mode at these position is unfavorable as they lie closer to the antenna. In the beginning of this section we have mentioned that also frequency spacing between the modes plays an important role in selectivity. Comparing the spectra obtained from the same surface shape but differently excited (Figure 5.4), we observe that exciting the mode non-centrally to get the HG modes leads to double the amount of excited modes and thus to half the frequency spacing between the individual modes.

Thus, two aspects play a role in the overall selectivity: the spatial and the frequency selectivity. The spatial selectivity from Figure 5.9 performs slightly better for the (1,0)-HG mode, but overall rather poorly. Yet, in terms of frequency selectivity, the (1,0)-LG mode outperforms the (1,0)-HG mode. Considering the poor spatial selectivity for both modes, it is eventually more advisable to aim for better frequency selectivity.
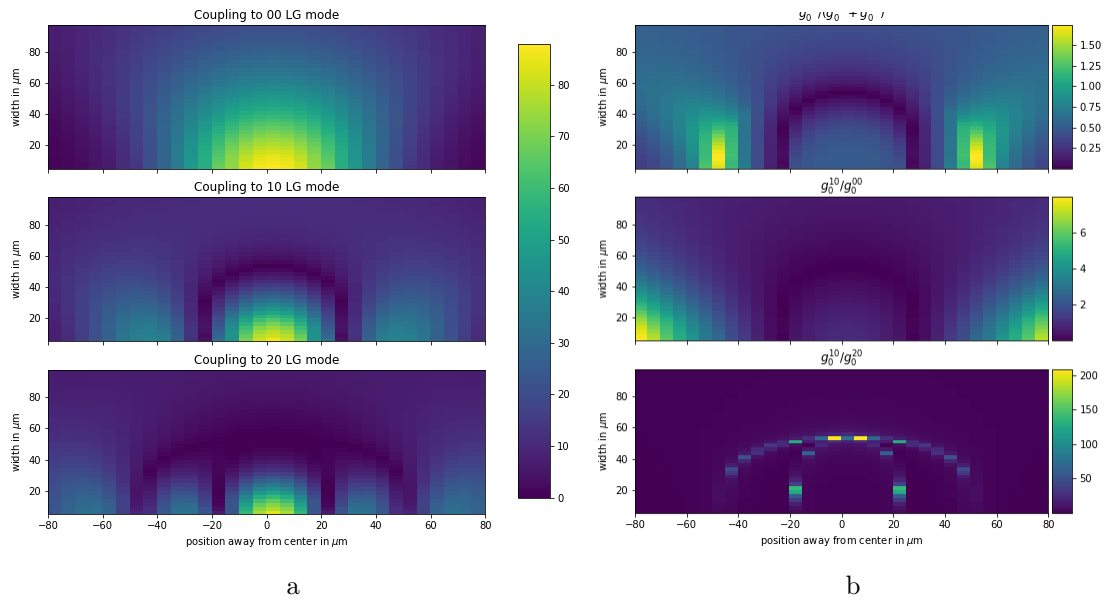

a   b

Figure 5.9.: **a)** Single photon optomechanical coupling rate to the (0,0)-, (1,0) and (2,0)-LG mode for different optical mode positions and waist sizes. **b)** Ratio of single photon optomechanical coupling rate to the (1,0)-LG mode divided by the sum of the coupling rates to the (0,0) and the (2,0) mode, only by the coupling rate to the (0,0) mode and only by the coupling rate to the (2,0) mode.

5.3. Quasiparticle Generation Rate on Antenna

In section 2.4 we have seen many negative effects of laser light shining onto a superconductor. By using the two-part (1,0)-LG mode and the (1,0)-HG mode we hope to reduce the absorbed laser power on the antenna. Here we will check how well this works and we will briefly look in general at what distance away the antenna would be best to keep the local quasiparticle generation rate $g(r)$ on the antenna below some threshold.

To determine the quasiparticle generation rate on the antenna we need to specify the input laser power. Regarding microwave to optical transduction, we aim to achieve a cooperativity C greater than one (as we have seen in section 2.2.6). For comparing the different designs from above, we set the laser power of each design such that we get a cooperativity $C > 1$ (see equation 2.33).

For each setup we examine the total absorbed laser power, the resulting average laser power per area, and we look at what distance from the laser center superconductivity stops breaking locally. This happens when the local generation rate exceeds a value of $g_s = 5.5 \cdot 10^{24}$ m^{-2}s^{-2}. We will call this distance the critical radius.

5.3.1. Comparing (1,0)-Hermite- and (1,0)-Laguerre-Gaussian Mode

Using the (1,0)-HG mode allows us to couple one part of the mode with the optical modes and one part with the electric field of the antenna from the superconducting qubit. The observations in Yu Yang's master's thesis [30] suggest to use a circular antenna to couple to one part of the (1,0)-HG mode.

For a laser waist of $w_{\mathrm{op}} = 20$ μm and the (1,0)-HG mode from Figure 5.1d we reach an optomechanical coupling rate of $98 \cdot 2\pi$ Hz. To achieve a cooperativity greater than one we thus need a laser input power of $P_{\mathrm{in}} = 13$ μW. At this laser power and for this waist size we get a critical radius of 33 μm.

Figure 5.10 shows the critical radius (red) in relation to the position of the antenna (brown) for the antenna setup from section 5.1. This antenna setup offers an electromechanical coupling of $g^{\mathrm{em}} = 351 \cdot 2\pi$ kHz with an antenna radius of 26 μm. Yet the number of quasiparticles created cannot be determined by the distance from the antenna only, but also depends on the laser power absorbed by the antenna. In this case, the total absorbed laser power is $P_{\mathrm{abs}} = 111$ nW. As quasiparticles are assumed to be in motion, we shall consider also the absorbed power per area. Here, there is a mean intensity of $I_{\mathrm{mean}} = 52$ W/m^2.
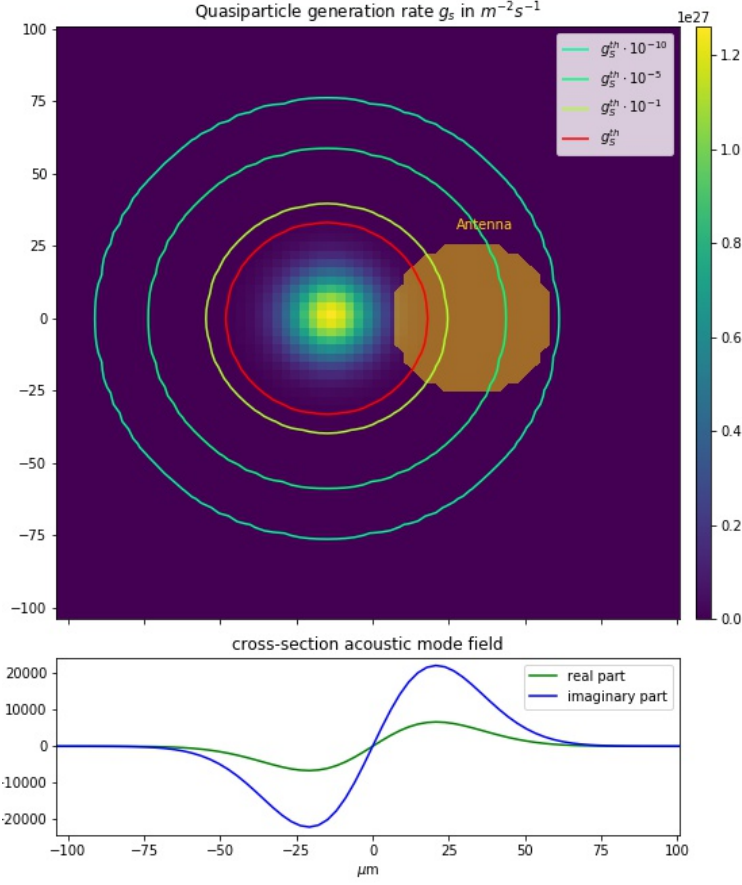
Figure 5.10.: Quasiparticle generation rate on a antenna ($r = 26\ \mu$m) placed $47.5\ \mu$m away from the position of the laser with waist $15\ \mu$m and $P_{\text{tot}} = 12.78$ μW. On the antenna the absorbed power is $P_{\text{abs}} = 111$ nW and the mean intensity $I_{\text{mean}} = 52$ W/m^2.

In the setup that utilizes the (1,0)-LG mode the laser shines onto the middle part of the mode. The electric field is produced by a ring shaped antenna and couples to the outer part of the LG mode.

As before, we set the laser waist to its minimum of $w_{\text{op}} = 20\ \mu$m and shine it centered onto the mode in Figure 5.1e. This way we reach a single photon coupling rate of $g_0^{\text{om}} = 92 \cdot 2\pi$ Hz. Thus, to reach a cooperativity greater than one, an input power of $P_{\text{in}} = 15\ \mu$W is needed. Superconductivity therefore breaks at a critical radius of $34\ \mu$m.

The critical radius is shown in Figure 5.11. It shows again the situation with the antenna

that leads to a strong coupling of $g^{\mathrm{em}} = 1143 \cdot 2\pi$ kHz, while having the inner radius of the antenna as large as possible. The total absorbed laser power is $P_{\mathrm{abs}} = 0.6$ nW which is smaller than in the antenna setup of the HG mode. Divided by the antenna area we get a mean intensity of $I_{\mathrm{mean}} = 0.2$ W/m^2.
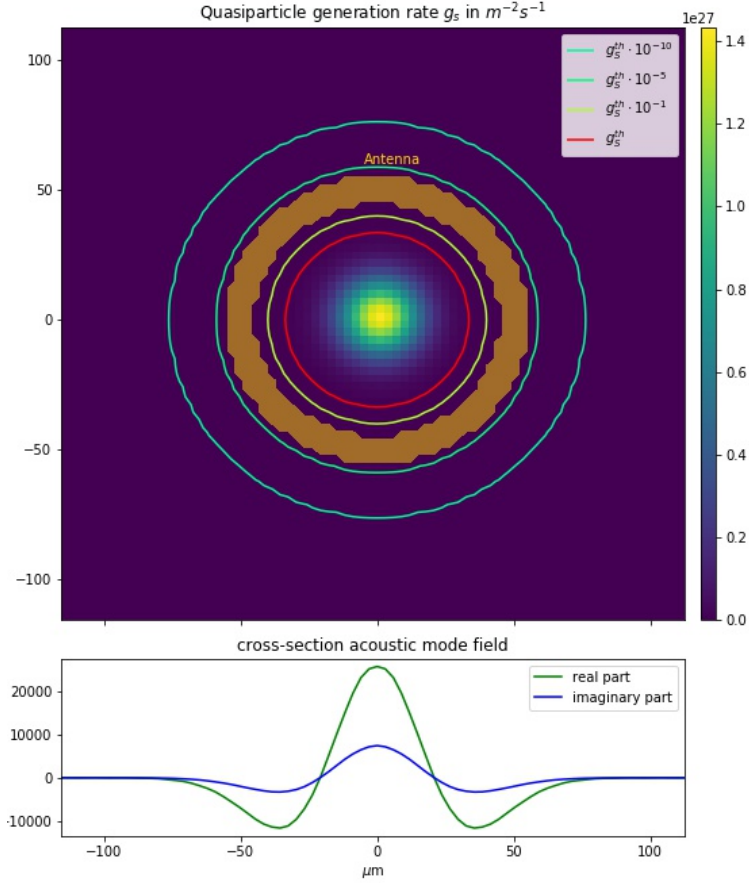

Figure 5.11.: Quasiparticle generation rate on a antenna ($r_{\mathrm{small}} = 45$ μm and $r_{\mathrm{large}} = 55$ μm) placed around the laser with waist 20 μm and $P_{\mathrm{tot}} = 15$ μW. On the antenna the absorbed power is $P_{\mathrm{abs}} = 0.6$ nW and the mean intensity $I_{\mathrm{mean}} = 0.2$ W/m^2.

In terms of quasiparticle generation on the antenna, the setup with the (1,0)-LG mode seems to perform an order of magnitude better. This is mainly because the distance of the antenna edge to the center of the laser is larger in the case of the (1,0)-LG mode.

5.3.2. Dependence of Laser Position and Width on Generation Rate

The size of the critical radius depends on the laser power and on the beam waist. Figure 5.12 shows how the radius changes as we adjust these two parameters. We observe that the laser waist plays a much more important role than the laser power. Hence, decreasing the laser waist not only increases the optomechanical coupling but also decreases the amount of absorbed laser power on the antenna. You can find the derivation for the waist dependence and power dependence of the critical radius in the Appendix A.5.
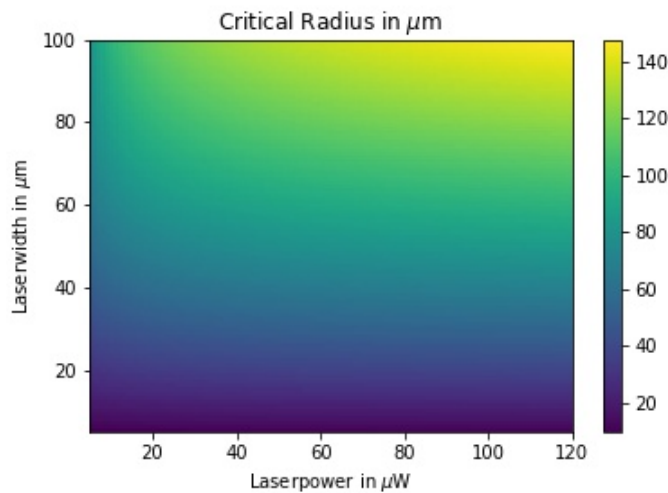
Figure 5.12.: Critical radius where superconductivity stops breaking as a function of laser power and laser waist.

5.4. Mode Shape Adjusting

Up to this point, we have only looked at the HG modes created by a spherically symmetric dome on the HBAR surface. A significant advantage the HG modes offer is that they can also occur when we fabricate an ellipsoidal HBAR surface. An ellipsoidal HBAR surface provides us more parameters to customize the acoustic mode shape. Further, we have seen that for ellipsoidal surfaces the two individual parts of the (1,0)-HG mode approximate more closely a Gaussian distribution than they do in the spherical dome.

To verify this, we simulate the modes of an HBAR with an ellipsoidal surface having parameters similar to the dome from above. The dome from above was simulated as the cut through a sphere with a radius $r = 65$ cm. For the ellipsoidal surface we again take the cut, but this time from an ellipsoid. An ellipsoid can be described using the length of the three principal axis a, b and c, where we cut along a plane perpendicular to the c-axis. To create a more comparable situation, we choose the axis length similar to the radius of the sphere from above. Namely: $a = 65$ cm, $b = 40$ cm and $c = 65$ cm.

Using this ellipsoidal surface and a laser waist of $w_{op} = 20$ μm we get a maximal single-photon optomechanical coupling rate of $g_0^{om} = 103 \cdot 2\pi$ Hz. In Appendix A.7.3, the corresponding surface, the spectrum and the modes are shown. To get a cooperativity greater than one, an input laser power of $P_{in} = 11.45$ μW is needed. Using a circle antenna with radius $r = 22$ μm and placing it at a distance of 27.5 μm left of the center seems to offer a good trade-off between increasing electromechanical coupling and decreasing quasiparticle generation. It then leads to an electromechanical coupling of $328 \cdot 2\pi$ kHz.

Figure 5.13 shows the critical radius we get for this setup. Comparing this to the setup of the (1,0)-HG mode from above we notice that the optomechanical coupling increases for an ellipsoid surface shape but the absorbed laser power and the mean intensity on the antenna stays on a similar level.

Knowing now that a surface ellipsoid changes the shape of HG modes, we can ask how strongly we can manipulate it. For this purpose, we simulated the shape of the (1,0)-HG mode for different surface ellipsoids. To keep fabrication simple, we set the c-axis of these ellipsoids to 22 cm. In Figure 5.14a we additionally kept the shorter b-axis constant at 15 cm and in Figure 5.14c we did it the other way around and kept the long a-axis at 35 cm and swept the short b-axis.

For the (1,0)-HG mode shapes, we evaluated four quantities: The distance of the maximum and the minimum (red) and the distances from the maximum to $1/e$ of the maximum value of the field to the top (grey), to the middle (blue) and to the left (green). We notice that by making the long axis a longer, the distance between the maximum and the minimum becomes larger, and by making the short axis b longer, we get larger widths to the top.

For increasing optomechanical coupling we aim for smaller mode waists and for decreasing the generation of quasiparticles a larger distance between the maximum and the minimum is needed. In Figure 5.14b and Figure 5.14d we show the ratio of the distance between the maximum and the minimum divided by the mean width. We defined the mean width as the arithmetic mean of the width to the left, the width to the middle and twice the width to the top (as the width to the top and the bottom are identical). In other words, we see that we get the best mode shapes for the smallest possible short axes b and the largest possible long axes a. However, the improvement here is only small and we still must ensure that stable modes can be build up from the surface shape.
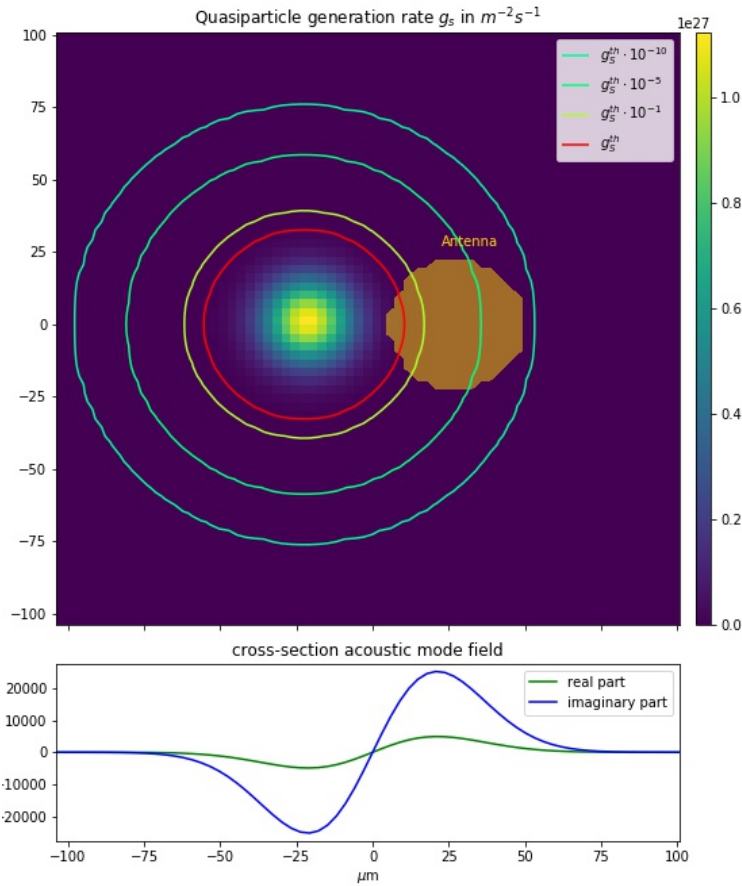
Figure 5.13.: Quasiparticle generation rate on a antenna ($r = 22$ μm) placed 42.5 μm away from the position of the laser with waist 15 μm and $P_{\text{tot}} = 11$ μW. On the antenna the absorbed power is $P_{\text{abs}} = 21$ nW and the mean intensity $I_{\text{mean}} = 13$ W/m^2.
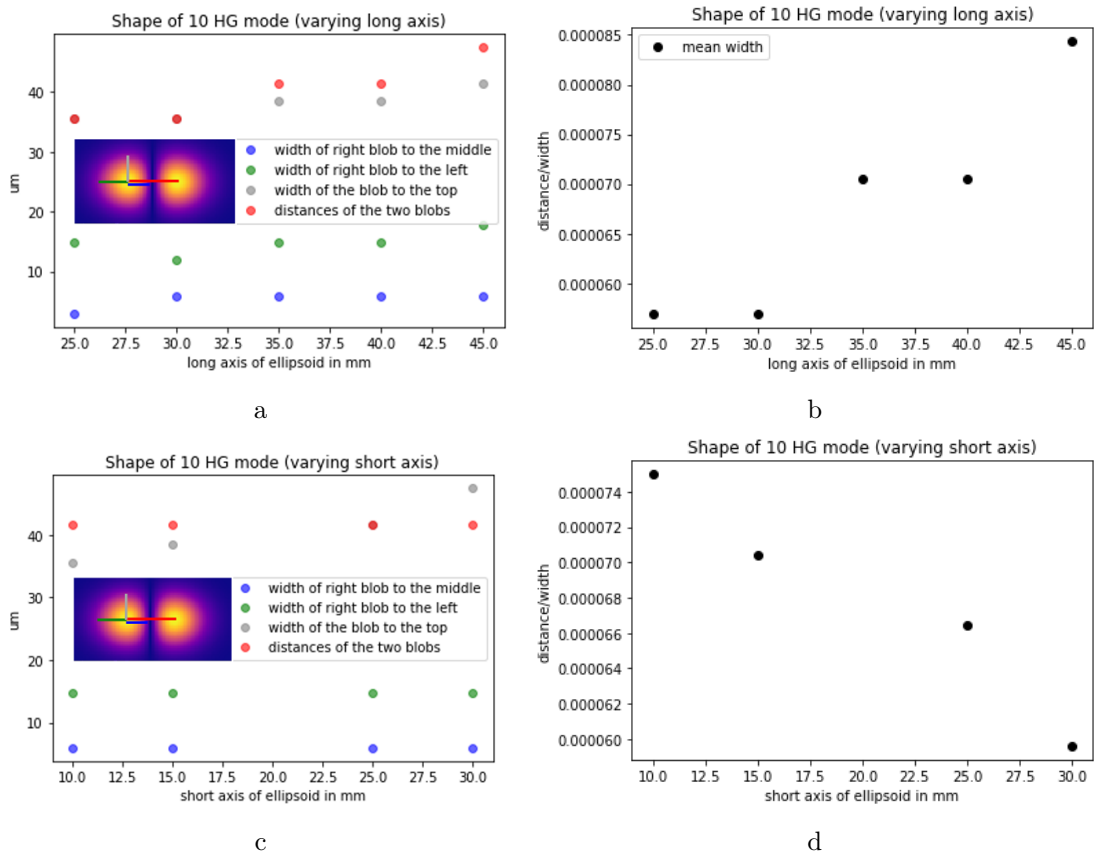
Figure 5.14.: **a)** Shape parameters when changing the long axis of the ellipsoid while keeping the short axis at 15 cm, **b)** Distance between the maximum and the minimum divided by the mean width of one part of the (1,0)-HG mode when changing the long axis of the ellipsoid (short axis: 15 cm), **c)** Shape parameters when changing the short axis of the ellipsoid while keeping the long axis at 35 cm, **b)** Distance between the maximum and the minimum divided by the mean width of one part of the (1,0)-HG mode when changing the short axis of the ellipsoid (long axis: 35 cm).

CHAPTER 6

Conclusion and Outlook

In this work, we have addressed several aspects that need to be considered when using HBAR-phonon modes for storing interim states in microwave to optical transduction: First, for increasing the electromechanical coupling of the phonon mode to the microwave photon, the shape and size of the superconducting antenna play an important role. Second, for increasing the optomechanical coupling between the phonon mode and the optical photon, we can lower the laser waist sizes and achieve ever larger coupling strengths. Here we are, however, limited in minimizing the laser waist by the distance between the pinhole, where the beam enters the microwave cavity, and the focus of the laser. Finally, for decreasing the quasiparticle generation on the superconducting antenna, we can mainly increase the distance between the laser center and the antenna and by again decreasing the laser waist. Additionally, we have seen that increasing the laser power does not lead to a large increase of the critical radius. Thus placing the antenna far away from the laser, we can increase the optomechanical coupling by increasing the laser power. This way we generate less additional quasiparticles on the antenna compared to a situation, where the antenna is placed closer to the laser. For this reason, it is important to be able to place the antenna far away from the laser.

For two different acoustic mode shapes - the (1,0)-HG mode and the (1,0)-LG mode - and appropriate antenna shapes, we have calculated certain key values. For the (1,0)-HG mode and a circle antenna with radius 26 μm we reach an electromechanical coupling strength of $351 \cdot 2\pi$ kHz. With a fixed optical mode waist of 20 μm, we need an input laser power of 12.8 μW to reach a cooperativity greater than one. This way, the antenna absorbs a total laser power of 111 nW. For the (1,0)-LG mode and a ring antenna we reach an electromechanical coupling strength of $1143 \cdot 2\pi$ kHz. Here, we need a input laser power of 14.5 μW to reach a cooperativity greater than one, which leads to 0.6 nW of absorbed laser power.

These values show us that microwave to optical transduction using HBAR-phonon modes for storing nterim states is indeed possible for both acoustic mode shapes. However, with respect to the key values considered here, the (1,0)-LG mode performs remarkably better. But the key values are not the only reasons why the (1,0)-LG modes seem to be more suitable: A central laser excitation leads on one hand to a less dense spectrum which increases both the electromechanical and the optomechanical selectivity and it leads on the other hand to an easier alignment of the laser onto the surface shape of the HBAR. Finally, we have shown in this thesis, if transduction efficiency is to be enhanced, which parameters are worth adjusting and which are not. For example, decreasing the laser waist yields to amplification of optomechanical coupling strength and reduction of quasi-

6. Conclusion and Outlook

particle generation on the antenna. It is important to mention that quantum transduction is a multi-parameter problem and we have considered only a limited subset of them here. In case certain parameters change substantially in the future, this work can be used as a guideline to find optimal acoustic modes.

Bibliography

1. Arute, F. *et al.* Quantum supremacy using a programmable superconducting processor. *Nature* **574.** `https://doi.org/10.1038/s41586-019-1666-5` (7779 Oct. 2019).

2. O'Brien, J. *et al.* Photonic quantum technologies. *Nature Photonics* **3.** `https://doi.org/10.1038/nphoton.2009.229` (12 Dec. 2009).

3. Kharel, P. *et al.* High-frequency cavity optomechanics using bulk acoustic phonons. *Science Advances* **5.** `https://doi.org/10.1126/sciadv.aav0582` (4 Feb. 2019).

4. Chu, Y. *et al.* Creation and control of multi-phonon Fock states in a bulk acoustic-wave resonator. *Nature* **563.** `https://doi.org/10.1038/s41586-018-0717-7` (Nov. 2018).

5. Chu, Y. *et al.* Quantum acoustics with superconducting qubits. *Science* **358.** `https://doi.org/10.1126/science.aao1511` (6360 Oct. 2017).

6. Renninger, W. H. *et al.* Bulk crystalline optomechanics. *Natrue Physics* **14.** `https://doi.org/10.1038/s41567-018-0090-3` (6 June 2018).

7. Gokhale, V. J. *et al.* Epitaxial bulk acoustic wave resonators as highly coherent multi-phonon sources for quantum acoustodynamics. *Nature Communications* **11.** `https://doi.org/10.1038/s41467-020-15472-w` (1 May 2020).

8. Kharel, P. *et al. Multimode strong coupling in cavity optomechanics* 2019. arXiv: `1812.06202 [physics.optics]`.

9. Lanz, D. & Eleiba, A. *The Good, the Bad and the Ugly: Social Media and Peace Mediation* (swisspeace Mediation Program, Dec. 2018).

10. Feynman, R. P. Simulating physics with computers. *Int. J. Theor. Phys.* **21,** 467–488 (1982).

11. Vepsäläinen, A. P. *et al.* Impact of ionizing radiation on superconducting qubit coherence. *Nature* **584.** `https://doi.org/10.1038/s41586-020-2619-8` (7822 Aug. 2020).

12. D. Royer E, D. *Elastic Waves in Solids I: Free and Guided Propagation* ISBN: 3-540-65932-3 (Springer, 1996).

13. *Departement of Phyiscs, Keio University* `http://www.phys.keio.ac.jp/guidance/labs/sasada/image/transverse.gif`. Accessed: 2021-01-08.

14. B. E. A. Saleh, M. C. T. *Fundamentals of Photonics* ISBN: 0-471-83965-5 (John Wiley Sons, Inc., 1991).

15. Kharel, P. *Utilizing Brillouin Interactions for Optical Control of Bulk Acoustic Waves* PhD thesis (Yale University, 2019).

Bibliography

16. M. Aspelmeyer T. J. Kippenberg, F. M. *Cavity Optomechanics: Nano- and Micromechanical Resonators Interacting with Light* ISBN: 978-3-642-55311-0 (Springer, 2014).

17. Bahl, G. *et al.* Observation of spontaneous Brillouin cooling. *Nature Physics* **8.** https://doi.org/10.1038/nphys2206 (3 Mar. 2012).

18. Zeuthen, E. *et al.* Figures of merit for quantum transducers. *Quantum Science and Technology* **3.** https://doi.org/10.1088/2058-9565/ab8962 (3 May 2020).

19. Chu, Y. *Lecture notes in Quantum Acoustics and Optomechanics* 2020.

20. W. P. Bowen, G. J. M. *Quantum Optomechanics* ISBN: 978-1-4822-5916-2 (Taylor Francis Group, LLC, 2016).

21. Aspelmeyer, M. *et al.* Cavity Optomechanics. *Rev. Mod. Phys.* **86.** https://link.aps.org/doi/10.1103/RevModPhys.86.1391 (4 Dec. 2014).

22. Arnau, A. *Piezoelectric Transducers and Applications* ISBN: 978-3-540-77507-2 (Springer, 2008).

23. Kaplan, S. B. *et al.* Quasiparticle and phonon lifetimes in superconductors. *Physical Review B* **14.** https://link.aps.org/doi/10.1103/PhysRevB.14.4854 (11 Dec. 1976).

24. Wang, C. *et al.* Measurement and control of quasiparticle dynamics in a superconducting qubit. *Nature Communications* **5.** https://link.aps.org/doi/10.1038/ncomms6836 (1 Dec. 2020).

25. Non-equilibrium quasiparticles in superconducting circuits: photons vs. phonons. *SciPost Physics.* preprints/scipost_201811_00008v2 (Dec. 2018).

26. Rajauria, S. *et al.* Efficiency of quasiparticle evacuation in superconducting devices. *Physical Review B* **85.** https://doi.org/10.1103/PhysRevB.85.020505 (2 Jan. 2012).

27. V. V. Schmidt P. Müller, A. V. U. *The Physics of Superconductors: Introduction to Fundamentals and Applications* ISBN: 978-3-642-08251-1 (Springer, 1997).

28. Soldini, M. *Quasiparticles dynamics under infrared illumination* Semester's thesis. 2019.

29. Kharel, P. *et al.* Ultra-high-Q phononic resonators on-chip at cryogenic temperatures. *APL Photonics* **3.** https://doi.org/10.1063/1.5026798 (6 June 2018).

30. Yang, Y. *Characterizing electromechanical coupling with multiplexed spectroscopy* Master's thesis. 2020.

Appendix

A.1. Normalization of Acoustic Mode

In order to calculate the overlap for the coupling strengths correctly, we must normalize the acoustic mode: For this we integrate the energy density of a single phonon mode over the whole HBAR and set it equal to the energy of a single phonon with the corresponding frequency ω_{ac}.

$$\int_V c_{33} \cdot |S(x,y,z)|^2 dV = \hbar\omega_{\text{ac}} \tag{A.1}$$

where c_{33} is the stiffness coefficient and $S(x,y,z)$ is the strain field. Using a as the normalization constant we want to find and $S(x,y,z) = a \cdot S_0(x,y)\sin(kz)$ we get:

$$
\begin{aligned}
\hbar\omega_{\text{ac}} &= c_{33}\int_\infty^\infty \int_\infty^\infty \int_0^{L_{\text{ac}}} a^2 |S_0(x,y)|^2 \sin^2(k_{\text{ac}}z) dx dy dz \\
&= c_{33}a^2 \underbrace{\int_\infty^\infty \int_\infty^\infty |S_0(x,y)|^2 dx dy}_{=A_m} \cdot \int_0^{L_{\text{ac}}} \sin^2(k_{\text{ac}}z) dz \\
&= c_{33}a^2 A_m \left[\frac{z}{2} - \frac{\sin(2k_{\text{ac}}z)}{4k}\right]_0^{z=L_{\text{ac}}} \\
&= c_{33}a^2 A_m \left[\frac{L_{\text{ac}}}{2} - \frac{\sin(2k_{\text{ac}}L_{\text{ac}})}{4k_{\text{ac}}}\right]
\end{aligned}
$$

Where L_{ac} is the length of the aocustic cavity. We thus find the normalization constant a:

$$a = \sqrt{\frac{2\hbar\omega_{\text{ac}}}{c_{33}A_m L_{\text{ac}}}} \tag{A.2}$$

Where we used the fact that $\sin(2k_{\text{ac}} \cdot L_{\text{ac}}) = 0$, since $2k_{\text{ac}} \cdot L_{\text{ac}} = 2 \cdot \frac{2\pi}{\lambda_{\text{ac}}} \cdot L_{\text{ac}} = m \cdot \pi$ for λ_{ac} of an acoustic mode and $m \in \mathbf{N}$.

A. Appendix

A.2. Normalization of Optical Mode

To calculate the overlap in the optomechanical coupling strength, we also need to normalize the optical modes. For this, we again integrate the energy density of a single mode over the optical cavity and set it equal to the energy of a single photon mode with corresponding frequency ω_0:

$$\hbar\omega_0 = \int_V \epsilon(r) \cdot |E(x,y,z)|^2 dV \tag{A.3}$$

$$\tag{A.4}$$

where $\epsilon(r)$ is the permittivity of the material. We again want to find the normalization constant b, where $E(x,y,z) = b \cdot E_0(x,y)\sin(kz)$. But here it is important to note, that we integrate over two different volumes: the vacuum and the HBAR.

$$
\begin{aligned}
\hbar\omega_0 =& \int_{-L_{\mathrm{ac}}}^{0} \int_{-\infty}^{\infty} \int_{-\infty}^{\infty} \epsilon_c \epsilon_0 b^2 E_0(x,y)^2 \sin^2(k_{\mathrm{mat}} z) dx dy dz \\
&+ \int_{0}^{d_0} \int_{-\infty}^{\infty} \int_{-\infty}^{\infty} \epsilon_0 b^2 E_0(x,y)^2 \sin^2(k_{\mathrm{vac}} z) dx dy dz \\
=& b^2 \epsilon_0 \Bigg[\epsilon_c \underbrace{\int_{-\infty}^{\infty} \int_{-\infty}^{\infty} E_0(x,y)^2 dx dy}_{=B_m} \cdot \int_{-L_{\mathrm{ac}}}^{0} \sin^2(k_{\mathrm{mat}} z) dz \\
&+ \underbrace{\int_{-\infty}^{\infty} \int_{-\infty}^{\infty} E_0(x,y)^2 dx dy}_{=B_m} \cdot \int_{0}^{d_0} \sin^2(k_{\mathrm{vac}} z) dz \Bigg] \\
=& b^2 \epsilon_0 B_m \Bigg[\epsilon_c \left[\frac{z}{2} - \frac{\sin\left(\frac{4\pi n}{\lambda_0} z\right)}{\frac{8\pi n}{\lambda_0}} \right]_{-L_{\mathrm{ac}}}^{z=0} + \left[\frac{z}{2} - \frac{\sin\left(\frac{4\pi}{\lambda_0} z\right)}{\frac{8\pi}{\lambda_0}} \right]_{0}^{z=d_0} \Bigg] \\
=& b^2 \epsilon_0 B_m \Bigg[\epsilon_c \left[\frac{L_{\mathrm{ac}}}{2} + \frac{\sin\left(-\frac{4\pi n}{\lambda_0} L_{\mathrm{ac}}\right)}{\frac{8\pi n}{\lambda_0}} \right] + \left[\frac{d_0}{2} - \frac{\sin\left(\frac{4\pi}{\lambda_0} d_0\right)}{\frac{8\pi}{\lambda_0}} \right] \Bigg] \\
=& b^2 \epsilon_0 B_m \Bigg[\epsilon_c \left[\frac{L_{\mathrm{ac}}}{2} - \frac{\lambda_0}{8\pi n} \sin\left(\frac{4\pi n}{\lambda_0} L_{\mathrm{ac}}\right) \right] + \left[\frac{d}{2} - \frac{\lambda_0}{8\pi n} \sin\left(\frac{4\pi}{\lambda_0} d_0\right) \right] \Bigg] \\
=& b^2 \epsilon_0 B_m \left[\epsilon_c \frac{L_{\mathrm{ac}}}{2} + \frac{d_0}{2} \right] \\
=& \frac{1}{2} b^2 \epsilon_0 B_m (L_{\mathrm{ac}}(\epsilon_c - 1) + L_{\mathrm{op}})
\end{aligned}
$$

Where k_{vac} and k_{mat} are the optical wavevectors in the vacuum and in the HBAR material, ϵ_c is the relative permittivity of the HBAR material and λ_0 is the vacuum wavelength. In the first step, we split the integration over the length of the optical cavity L_{op} into an

integration over the crystal length L_{ac} and over the length of the optical cavity without a crystal $d_0 = L_{op} - L_{ac}$. In the last step we used the fact that the acoustic and the optical waves are standing modes of the acoustic and the optical cavity:

$$
\begin{aligned}
k_{ac} L_{ac} &= \frac{2\pi}{\lambda_{ac}} \cdot L_{ac} \\
&= \frac{2\pi}{1/2\lambda_{op}} \cdot L_{ac} \\
&= \frac{4\pi n}{\lambda_0} \cdot L_{ac} \\
&= q \cdot \pi
\end{aligned}
$$

where λ_{op} is the optical wavelength in the material, λ_0 the vacuum wavelength, n the refractive index of the material and $q \in \mathbf{N}$. And we also used the fact that:

$$
\begin{aligned}
s\pi &= k_{op} \cdot L_{ac} + k_0 \cdot d_0 \\
&= \frac{2\pi}{\lambda_{op}} \cdot L_{ac} + \frac{2\pi}{\lambda_0} \cdot d_0 \\
&= \underbrace{\frac{2\pi n}{\lambda_0} \cdot L_{ac}}_{=\frac{q}{2}\pi} + \frac{2\pi}{\lambda_0} \cdot d_0
\end{aligned}
$$

where $s \in \mathbf{N}$. The last term then also needs to be $l/2 \cdot \pi$, where $l \in \mathbf{N}$ and therefore $\sin\left(\frac{4\pi}{\lambda_0} \cdot d_0\right) = 0$. Thus, we have

$$
b = \sqrt{\frac{2\hbar\omega_0}{\epsilon_0 B_m} \cdot \frac{1}{L_{ac}(\epsilon_c - 1) + L_{op}}} \tag{A.5}
$$

A.3. Overlap of three Gaussian functions

Having a fixed acoustic mode with a gaussian shape and a width W_{ac}, we want to know the width W_{op} of the optical modes so that the optomechanical coupling is maximized. For this we analyse the overlap integral of the three gaussians from equation 2.37.
In a first step we normalize the gaussians, so their integral over the xy-plane is equal to one. For this we take a gaussian:

$$
f(x) = a \cdot \exp\left(-\frac{x^2 + y^2}{W^2}\right)
$$

47

where a is the normalization constant we are looking for.

$$\int_{-\infty}^{\infty}\int_{-\infty}^{\infty} a^2 \cdot \exp\left(-2\frac{x^2+y^2}{W^2}\right)dxdy = 1$$

$$a^2 \cdot \int_{-\infty}^{\infty}\exp\left(-2\frac{x^2}{W^2}\right)dx \cdot \int_{-\infty}^{\infty}\exp\left(-2\frac{y^2}{W^2}\right)dy = a^2\frac{W^2\pi}{2} = 1$$

gives us

$$a = \sqrt{\frac{2}{\pi W^2}}.$$

Calculating the overlap:

$$O = \int_{-\infty}^{\infty}\int_{-\infty}^{\infty} f_{\text{ac}}(x,y) \cdot f_j(x,y) \cdot f_{j+1}(x,y)dxdy$$

$$= \int_{-\infty}^{\infty}\int_{-\infty}^{\infty} \frac{2}{\pi W_{\text{op}}^2}e^{-2\frac{x^2+y^2}{W_{\text{op}}^2}} \cdot \sqrt{\frac{2}{\pi W_{\text{ac}}^2}}e^{-\frac{x^2+y^2}{W_{\text{ac}}^2}}\,dxdy$$

$$= \sqrt{\frac{8}{\pi^3 W_{\text{op}}^4 W_{\text{ac}}^2}}\int_{-\infty}^{\infty} e^{-\left(\frac{2}{W_{\text{op}}^2}+\frac{1}{W_{\text{ac}}^2}\right)x^2}\,dx \cdot \int_{-\infty}^{\infty} e^{-\left(\frac{2}{W_{\text{op}}^2}+\frac{1}{W_{\text{ac}}^2}\right)y^2}\,dy$$

$$= \sqrt{\frac{8}{\pi^3 W_{\text{op}}^4 W_{\text{ac}}^2}}\frac{\pi}{\frac{2}{W_{\text{op}}^2}+\frac{1}{W_{\text{ac}}^2}}$$

$$= \sqrt{\frac{8}{\pi^3 W_{\text{op}}^4 W_{\text{ac}}^2}}\frac{\pi W_{\text{op}}^2 W_{\text{ac}}^2}{2W_{\text{ac}}^2 + W_{\text{op}}^2}$$

$$= \sqrt{\frac{8}{\pi}} \cdot \frac{W_{\text{ac}}}{2W_{\text{ac}}^2 + W_{\text{op}}^2}$$

We see that O goes to infinity as W_{op} goes to 0. Therefore the overlap of the increases as the width of the optical gaussians goes to zero.

A.4. Crystal Position

The optomechanical coupling strength depends on the position of the HBAR inside the optical cavity. To find the optimal position, we take a look at the optomechanical coupling strength in the supplementary information of [3]:

$$g_0^{\text{om}} = A\epsilon_0\epsilon_r^2 p_{13}k_{\text{ac}}\sqrt{\frac{\hbar}{\rho AL_{\text{ac}}\Omega_{\text{ac}}}}\frac{\sqrt{\omega_j\omega_{j+1}}}{\epsilon_0\epsilon_r^{\text{eff}}AL_{\text{op}}} \cdot$$

$$\int_d^{d+L_{\text{ac}}} \sin\left(k'_{j+1}(z-d+\frac{d}{n})\right)\sin\left(k'_j(z-d+\frac{d}{n})\right)\sin(k_{\text{ac}}(z-d))dz$$

where d is the position of the crystal inside the optical cavity, ϵ_r^{eff} is defined by $\epsilon_r^{eff} * L_{\mathrm{op}} = L_{\mathrm{ac}}(\epsilon_c - 1) + L_{\mathrm{op}}$ and A is the optical and acoustic mode area (they are assumed to be the same here). Using the identity S19 and the phase matching condition $k_{\mathrm{ac}} = k'_{j+1} + k'_j$ gives us:

$$
\begin{aligned}
g_0^{\mathrm{om}} =& A\epsilon_0\epsilon_r^2 p_{13}k_{\mathrm{ac}}\sqrt{\frac{\hbar}{\rho AL_{\mathrm{ac}}\Omega_{\mathrm{ac}}}}\frac{\sqrt{\omega_j\omega_{j+1}}}{\epsilon_0\epsilon_r^{\mathrm{eff}}AL_{\mathrm{op}}} \cdot \\
& \int_d^{d+L_{\mathrm{ac}}} \frac{1}{4}\Big(-\sin\Big((z-d)(-2k'_j) + \frac{d}{n}(k'_{j+1}-k'_j)\Big) + \sin\Big(\frac{d}{n}k_{\mathrm{ac}}\Big) \\
& + \sin\Big(-(z-d)(2k'_{j+1}) + \frac{d}{n}(k'_{j+1}-k'_j)\Big) + \sin\Big((z-d)2k_{\mathrm{ac}} + \frac{d}{n}k_{\mathrm{ac}}\Big)\Big)dz \\
=& A\epsilon_0\epsilon_r^2 p_{13}k_{\mathrm{ac}}\sqrt{\frac{\hbar}{\rho AL_{\mathrm{ac}}\Omega_{\mathrm{ac}}}}\frac{\sqrt{\omega_j\omega_{j+1}}}{\epsilon_0\epsilon_r^{\mathrm{eff}}AL_{\mathrm{op}}} \cdot \frac{1}{4}\Big[\\
& -\frac{1}{2k'_j}\Big(\cos\Big(\frac{d}{n}(k'_{j+1}-k'_j) - 2k_jL_{\mathrm{ac}}\Big) - \cos\Big(\frac{d}{n}(k_{j+1}-k_j)\Big)\Big) \\
& + L_{\mathrm{ac}}\sin\Big(\frac{d}{n}k_{\mathrm{ac}}\Big) \\
& + \frac{1}{2k'_{j+1}}\Big(\cos\Big(\frac{d}{n}(k'_{j+1}-k'_j) - 2k_{j+1}L_{\mathrm{ac}}\Big) - \cos\Big(\frac{d}{n}(k_{j+1}-k_j)\Big)\Big) \\
& + \frac{1}{2k'_j}\Big(\cos\Big(2L_{\mathrm{ac}}k_{\mathrm{ac}} + \frac{d}{n}k_{\mathrm{ac}}\Big) - \cos\Big(\frac{d}{n}k_{\mathrm{ac}}\Big)\Big)\Big] \\
\approx& A\epsilon_0\epsilon_r^2 p_{13}k_{\mathrm{ac}}\sqrt{\frac{\hbar}{\rho AL_{\mathrm{ac}}\Omega_{\mathrm{ac}}}}\frac{\sqrt{\omega_j\omega_{j+1}}}{\epsilon_0\epsilon_r^{\mathrm{eff}}AL_{\mathrm{op}}} \cdot \frac{L_{\mathrm{ac}}}{4}\sin\Big(\frac{d}{n}k_{\mathrm{ac}}\Big)
\end{aligned}
$$

Therefore we get maximal coupling rate for

$$
d = \frac{\pi n}{2k_{\mathrm{ac}}}
$$

A.5. Critical Radius

Local quasiparticle generation increases with IR-laser intensity. For a Gaussian laser beam, the intensity is Gaussian distributed and decreases exponentially from the center of the beam. From equation 2.40 we know:

$$
I(x,y,z) = \frac{2P_0}{\pi w_0^2}\left(\frac{w_0}{w(z)}\right)^2 \exp\left(\frac{-2(x^2+y^2)}{w(z)^2}\right) \tag{A.6}
$$

We will ideally focus on the flat side of the HBAR. However, as the length of the crystal is smaller than the Rayleigh length of the laser beam, we can consider the situation on

the antenna at $z = 0$:

$$I(x, y) = \frac{2P_0}{\pi w_0^2} \exp\left(\frac{-2(x^2 + y^2)}{w_0^2}\right) \tag{A.7}$$

$$= \frac{2P_0}{\pi w_0^2} \exp\left(\frac{-2r^2}{w_0^2}\right) \tag{A.8}$$

where we defined the radius r as the distance from the center of the laser beam. The local quasiparticle generation rate can now be defined as:

$$g_s(r) = \frac{I(r)}{\epsilon} \tag{A.9}$$

$$= \frac{2P_0}{\pi w_0^2 \epsilon} \exp\left(\frac{-2r^2}{w_0^2}\right) \tag{A.10}$$

where ϵ is defined in equation 2.38. Martina Soldini [28] has shown, that at a value of $g_s^{th} = 5.5 \cdot 10^6$ μm^{-2} μs^{-1} the number of quasiparticles reaches the number of Cooper pairs and we have superconductivity breaking. We can therefore find a radius r_{th} at which the quasiparticle generation rate reaches this value and there is superconductivity breaking:

$$g_s^{th} = \frac{2P_0}{\pi w_0^2 \epsilon} \exp\left(\frac{-2r_{th}^2}{w_0^2}\right) \tag{A.11}$$

Which leads to:

$$r_{th} = \sqrt{\frac{1}{2}w_0^2 \cdot \ln\left(\frac{2P_0}{g_s^{th}\pi w_0^2 \epsilon}\right)} \tag{A.12}$$

We thus see, the critical radius depends on the laserwaist w_0 and the input laser power P_0.

A.6. Limited Optical Waist Size

A Gaussian beam's amplitude in the transversal plane is Gaussian distributed with waist $w(z)$. Along the axis of propagation this waist changes according to:

$$w(z) = w_0\sqrt{1 + \left(\frac{z}{z_R}\right)^2} \tag{A.13}$$

with the Rayleigh length z_R:

$$z_R = \frac{\pi w_0^2 n}{\lambda_0} \tag{A.14}$$

As we want to go lower in optical waist size we are now limited due to the cavity geometry: In the cavity geometry we shoot the laser beam through a pinhole with radius of approximately 1.5 mm. Around 2 cm behind the pinhole lies the focus with waist w_0. As we go lower in waist at the focus w_0, the waist at the pinhole $w(z = 2 \text{ cm})$ increases. We therefore need to find the minimal waist w_0, which allows us to pass the most part of the laser beam trough the pinhole.

Aiming for a waist at the hole of 0.5 mm, we get a focus waist size of 20 μm. However, it should be noted here that the 2cm between the hole and the focus is rather large, and it would probably also work with 1 cm. So you could also try a smaller waist size at the focus.

Additionally, by changing the optical waist size, the radius of curvature of the beam front changes as well. To adapt the system to the changed radius of curvature, it is necessary to find suitable mirrors. However, at a distance of 2cm the radius of curvature does not change too much and suitable mirrors can be found for a wide range of different waist sizes.

A.7. BeamProp Simulations

A.7.1. Dome Surface Laguerre Gaussian Modes
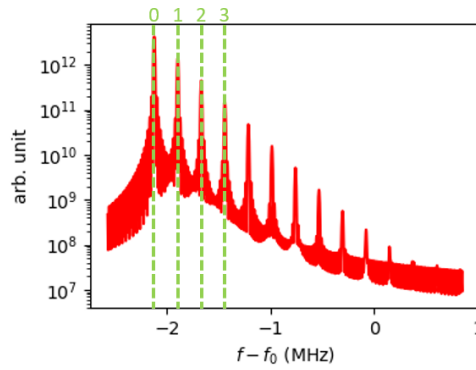
a Spectrum
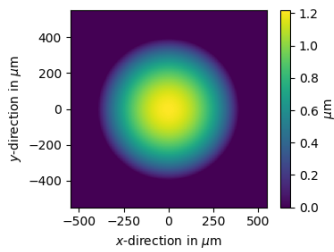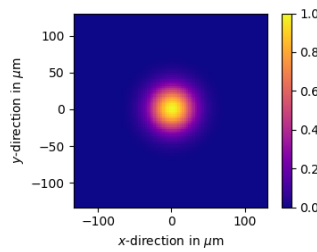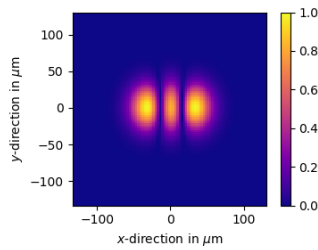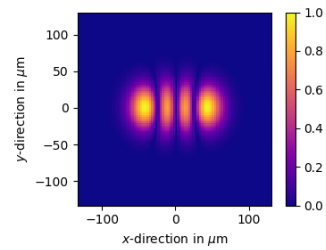

b HBAR surface

c Mode 0, (0,0)-LG Mode
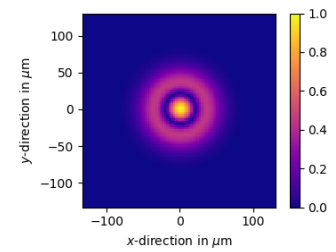
d Mode 1, (1,0)-LG Mode
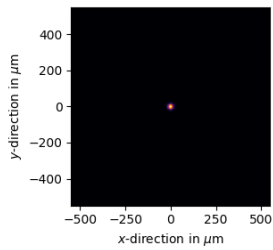
e Initial Excitation Field
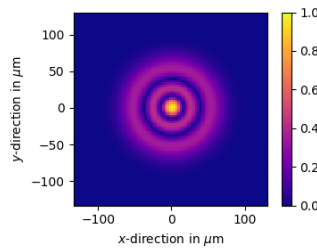
f Mode 2, (2,0)-LG Mode
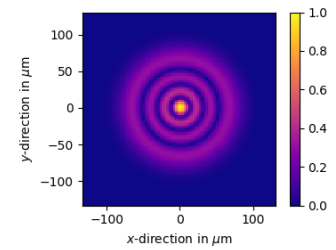
g Mode 3, (3,0)-LG Mode

A.7.2. Dome Surface Hermite Gaussian Modes
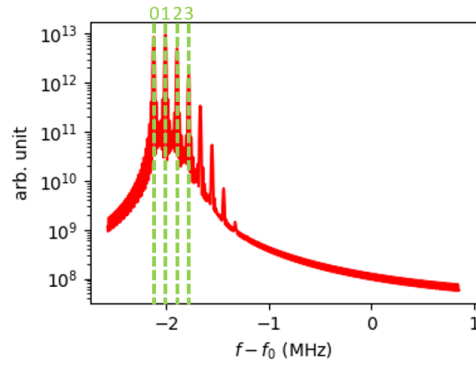
a Spectrum
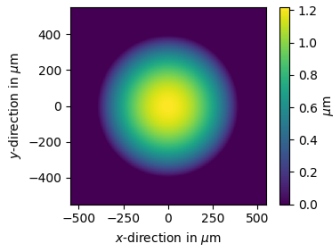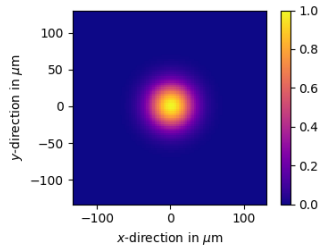
b HBAR surface
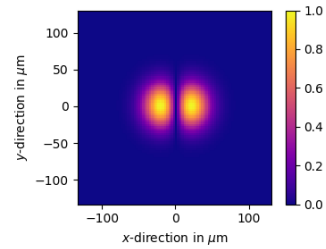
c Mode 0, (0,0)-HG Mode
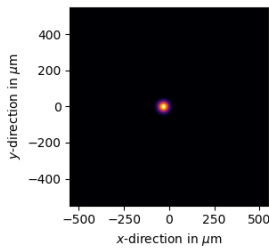
d Mode 1, (1,0)-HG Mode
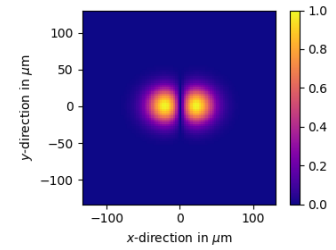

e Initial Excitation Field

f Mode 2, (2,0)-HG Mode

g Mode 3, (3,0)-HG Mode

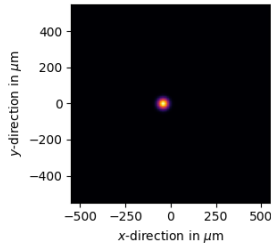### A.7.3. Ellipsoid Surface
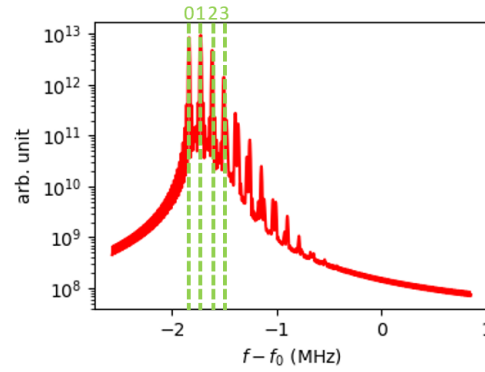
a Spectrum
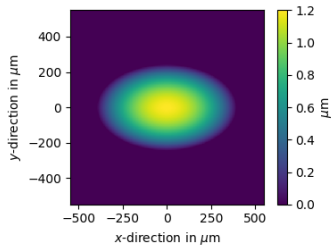
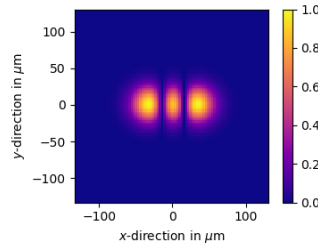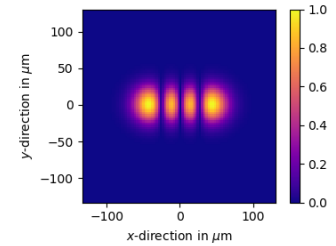

b HBAR surface
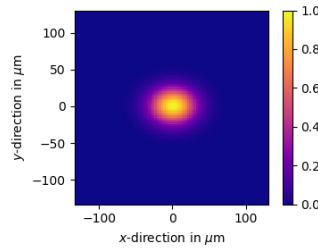
c Mode 0, (0,0)-HG Mode

d Mode 1, (1,0)-HG Mode

e Initial Excitation Field

f Mode 3, (2,0)-HG Mode

g Mode 4, (3,0)-HG Mode

A.7.4. Simulation parameters

Here are the parameters listed we used for the simulation:

Parameter	Value	Comment
Brillouin frequency	$13.4 \cdot 10^9$ Hz	of CaF_2
Longitudinal sound velocity	7204 m/s	in CaF_2
HBAR length	420 μm	wafer thickness
Exponential Correction Factor	2.473	corrects for the slowness surface